

## Revised structure models for antigorite: An HRTEM study

ISTVÁN DÓDONY,<sup>1,\*</sup> MIHÁLY PÓSFAL,<sup>2</sup> AND PETER R. BUSECK<sup>1</sup>

<sup>1</sup>Departments of Geological Sciences and Chemistry/Biochemistry, Arizona State University, Tempe, Arizona 85287, U.S.A.

<sup>2</sup>Department of Earth and Environmental Sciences, University of Veszprém, H-8201, Veszprém, Hungary

### ABSTRACT

We have revised the structure model of antigorite so that they conform to observations made using high-resolution transmission electron microscopy (HRTEM) images and selected-area electron diffraction. The new models retain the original half-wave configuration proposed by Kunze (1956). The Kunze model, and all subsequent research, assumes the occurrence of four- and eight-membered silicate rings in one of the two places where there are reversals of tetrahedron orientations in the tetrahedral sheets. However, TEM images at sufficiently high resolution show no traces of such rings and only half the number of octahedral-sheet offsets as occur in the Kunze model. Using our measurements and models, we generated atom positions for antigorite unit cells having various modulation lengths and then calculated the corresponding images, which provide good matches with our experimental HRTEM images. We also characterized and described antigorite structures with different modulation wavelengths and stacking sequences. Depending on the number of polyhedra in a unit cell and the presence or absence of  $b/3$  shifts between adjoining tetrahedral and octahedral sheets, the antigorite crystals have monoclinic or triclinic symmetry, which we call antigorite-*M* and antigorite-*T*, respectively. By resolving the tetrahedral and octahedral positions, we were able to make a direct estimate of the compositions of specific antigorite samples.

### INTRODUCTION

The serpentines are widespread hydrous, aseismic, rock-forming minerals (RFM) that play major roles in tectonic processes. They are important in some subduction zones and provide an explanation for the surprising fact that certain forearc seismic zones end at the Moho rather than extending deeper into the normally stronger mantle rocks (Peacock and Hyndman 1999). Much effort has been devoted to determining the strength and frictional behavior of these relatively weak minerals (Reinen et al. 1991, 1994; Moore et al. 1996, 1997), largely because of their association with major transform faulting and shear zones (Christensen 1972; Bonatti 1976; Francis 1981; O'Hanley 1996). Moreover, the serpentines are major carriers of water in subduction zones. Serpentinization results when the subducted oceanic crust releases fluids that infiltrate and alter the overlying mantle wedge (Hyndman et al. 1997) as well as during ocean floor spreading (Viti and Mellini 1998; Anselmi et al. 2000). Meteoric waters also generate serpentines and contribute to conditions that facilitate underthrusting and prograde metamorphism (Peacock 1987). On a different scale, they are important constituents of many primitive carbonaceous chondrite meteorites (Bunch and Chang 1980; Tomeoka and Buseck 1985, 1990; Buseck and Hua 1993; Zolensky et al. 1993; Brearley et al. 1999).

The structure and chemistry of serpentine minerals explain their important roles in tectonism, but there are many unresolved issues related to those structures and, to a lesser extent, compositions. No obvious link exists between the resolution of these structural issues and tectonic behavior, but we believe the questions are fundamental and relevant to these widespread, geologically important minerals.

Antigorite is notable among rock-forming minerals for its lack of a well-determined structure. For antigorite, Kunze (1958) proposed an alternating-wave structure model (Fig. 1) based on a 2D Fourier synthesis of  $h0l$  X-ray reflections. As discussed in the following section, most subsequent workers accepted this basic model. However, we found that it does not provide a satisfactory explanation for a number of observations: (1) the modulation directions in antigorite from Val Antigorio, Italy differ from those in the Kunze model (Dódony et al. 1998); (2) high-resolution transmission electron microscope (HRTEM) images do not show eight-membered rings that, if present, should be clearly visible in such images; (3) contrast mismatches exist between experimental HRTEM images and calculated images based on the Kunze model, indicating that it needs correction; and (4) the tetrahedral (T) and octahedral (O) positions are unresolved in published HRTEM images; thus, structural interpretations for differences in the observed  $(M^{2+}, M^{3+}):Si$  ratios (Viti and Mellini 1996; Wunder et al. 1997) between antigorite and  $Mg_3[Si_2O_5(OH)_4]$  (the hypothetical end-member lizardite composition) remain speculative until higher resolutions are achieved. The goals of this study are to resolve these antigorite structural and compositional ambiguities.

\* Permanent address: Department of Mineralogy, Eötvös L. University, Budapest, H-1117, Pázmány sétány 1C, Hungary. E-mail: dodony@ulixes.elte.hu

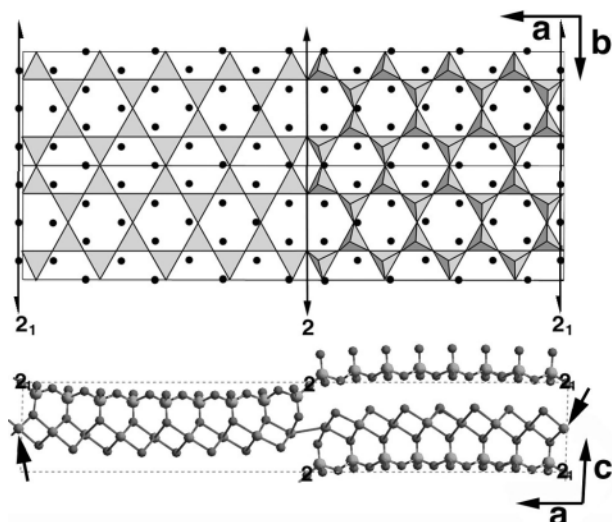


**FIGURE 1.** The Kunze (1958) model of antigorite as seen along [001] (top) and [010] (bottom). The black dots in the a-b projection represent the octahedrally coordinated positions. Reversals in the tetrahedral sheets occur at the indicated 2 and  $2_1$  axes (long arrows). As can be seen in the a-b projection, tetrahedra form alternating four- and eight-membered rings along the twofold axis. The light lines outline unit cells. The short arrows mark the positions of special O sites.

### STRUCTURE AND CHEMISTRY OF ANTIGORITE

The magnesian serpentine minerals antigorite, chrysotile, and lizardite are 1:1 trioctahedral phyllosilicates with the general formula  $(M_3^{2+}M_1^{3+})[(Si_{2-x}M_1^{3+})O_5(OH)_4]$ , where  $M^{2+} = Mg, Fe, Mn,$  and  $Ni$ , and  $M^{3+} = Al, Fe,$  and  $Cr$ . In antigorite the ratio of octahedral to tetrahedral cations is slightly smaller than in chrysotile and lizardite. Therefore antigorite cannot strictly be considered a serpentine polymorph (Wicks and Whittaker 1975); however, since it has close genetic, crystal-chemical, and structural relationships with the other two minerals, most researchers consider antigorite a serpentine polymorph.

Lizardite is the most abundant serpentine mineral and has the best understood structure. The antigorite structure is related to that of an idealized serpentine (Wicks and O'Hanley 1988), approximated by lizardite, which consists of alternating T and O sheets (Mellini 1982; Mellini and Zanazzi 1987; Mellini and Viti 1994; Krstanovic and Karanovic 1995). As a starting point we use idealized lizardite for the description of the structural details of antigorite. Slight shifts of the Mg positions and tetrahedral rotations were observed in studies of lizardite. However, we do not consider these features in the idealized structure because they result from the misfit between the T and O sheets, and in antigorite the misfit is mainly accommodated by the wave-like modulation and reversals of the T sheets.

The only direct structural information for antigorite consists of a two-dimensional Fourier synthesis of  $h0l$  reflections (Kunze 1958), rendering the existing model somewhat speculative. The dimensions of the T and O sheets do not match in serpentine minerals. In lizardite the T and O sheets can be compatible if Al substitutions occur at both the T and O positions (Thomas et al. 1979) or if the misfit is compensated by slight

adjustments of atomic positions. In antigorite, the misfits are primarily accommodated by reversals of the T sheets (Fig. 1), resulting in periodic modulations. These reversals occur at alternating [010] twofold screw axes and [010] twofold axes within the basal planes of the tetrahedra in the T sheets (Kunze 1956, 1958, 1961; Spinnler 1985; Uehara 1998). The silicate tetrahedra remain arranged in six-membered rings at the  $2_1$  axes, whereas four- and eight-membered rings reportedly occur at the twofold axes. Kunze termed this alternating-wave model the "double half-wave structure." The borders of the half-waves lie at the reversals of the T sheets, and the double half-wave defines the supercell and superstructure of antigorite. The atomic arrangement at the tetrahedral reversals imposes strict geometrical constraints on the curvature of the half-wave and the size of the supercell, as discussed in detail by Kunze (1961) and Wicks and Whittaker (1975).

The antigorite subcell is based on the orthohexagonal representation of the idealized lizardite unit cell but has a slightly longer  $a$  dimension and thicker octahedral sheet. In contrast to the 2:3 ratio of T and O positions in lizardite, the Kunze model requires a T:O ratio of 17:24 and implies that antigorite is Mg-deficient relative to lizardite. Wunder et al. (1997) successfully synthesized antigorite with a composition identical to the theoretical formula of  $Mg_{48}[Si_{34}O_{85}(OH)_{62}]$  deduced from the Kunze model. Because the stoichiometry at the reversals with four- and eight-membered rings differs from that of the rest of the structure, the composition of antigorite also depends on the length of the double half-wave, e.g., the size of the superlattice (Kunze 1961).

To refer to the various viewing directions of the antigorite structure it is convenient to use indices relating to either the subcell or the supercell. The relation is that  $[uvw]_{\text{subcell}}$  corresponds to  $[2u(n-1)v(n-1)w]_{\text{supercell}}$ , where  $n$  is equal to the number of T positions in a modulation period of antigorite when viewed along [010]. In this paper we generally refer to the subcell indices and directions except for the case of antigorite with  $n = 14$ , where it can be useful to refer to the supercell indices and directions, e.g.,  $[3\bar{1}6]_{\text{subcell}}$  and  $[\bar{3}16]_{\text{subcell}}$  are parallel to  $[6\bar{1}378]_{\text{supercell}}$  and  $[\bar{6}1378]_{\text{supercell}}$ , respectively.

In the last 15 years new details regarding the antigorite structure have been obtained from TEM studies. Spinnler (1985) and Mellini et al. (1987) observed the variability of its supercell size and suggested that these variations result from polysomatic alternations of lizardite six- and eight-membered modules of varied widths. Otten (1993) obtained the best high-resolution TEM images of [010] projections of antigorite published to date. He interpreted these images in agreement with Spinnler's structural interpretation, based on the principle of polysomatism (Thompson 1978), of the Kunze model.

Uehara (1998) obtained [001] HRTEM images of antigorite and calculated images using a coordinate set based on the Kunze model. He found good agreement between his experimental and simulated images. However, he did not recognize the non-orthogonal axes of [001] projections and used  $\gamma = 90^\circ$  in his image simulations. In addition, he matched the Kunze model ( $a = 43.3 \text{ \AA}$ ) with experimental images that had  $a = 35.5 \text{ \AA}$ . Therefore, the agreement between experimental and simulated micrographs of Uehara (1998) may be fortuitous.

Dódonny et al. (1998) concluded there is an absence of the eight-membered modules proposed in the antigorite model of Kunze, raising the possibility that a revised structure model is needed. They based their results on experimental [001] HRTEM images with better than 2 Å resolution. These images were filtered to eliminate noise, and then deconvoluted so that they clearly show the two types of sheets of coordination polyhedra.

### MATERIALS AND EXPERIMENTAL TECHNIQUES

We studied antigorite samples from Val Antigorio, Italy; Felsőcsatár, western Hungary; and Deligh quarry, Baltimore County, Maryland, U.S.A. The Val Antigorio sample is a foliated antigorite schist, and the other two specimens are of the splintery form of antigorite. The Val Antigorio and Deligh quarry samples are monomineralic, whereas fibrous talc is associated with antigorite in the Felsőcsatár specimen.

The samples were crushed under ethanol and deposited onto copper grids covered by lacey-carbon supporting films to obtain crystals lying on their basal (001) planes. To permit viewing perpendicular to [001], i.e., to observe the layering, Ar-ion milling was used on the Felsőcsatár and Deligh quarry samples. The thinned samples were lightly coated with carbon to avoid charging.

Energy dispersive X-ray spectrometry (EDS) analyses were made using a JEOL 2000FX (200 kV; side-entry, double-tilt stage;  $c_s = 2.1$  mm) transmission electron microscope with attached KEVEX X-ray detector. Spectra were processed and quantified using KEVEX QUANTEX software. Oxygen was not measured and the results were normalized to 100%. The results of the EDS measurements are given in Table 1.

A JEOL 4000EX (400 kV; top-entry, double-tilt stage;  $c_s = 1$  mm) transmission electron microscope was used for HRTEM imaging. Crystals were aligned along their crystallographic axes. The antigorite subcell reflections are intense and form a reciprocal lattice similar to that in 1:1 sheet silicates. We aligned the crystals by maximizing the intensities of both superlattice and subcell reflections.

Diffraction patterns for the high-resolution micrographs were calculated using Gatan Digital Micrograph 2.5.7 software (Meyer et al. 1996) to check the experimental conditions (crystallographic orientation, resolution, and astigmatism). The statistical nature of image formation in the microscope and the photo processing cause random noise in the experimental images. Additionally, the carbon coating, the presence of an amorphous surface layer caused by ion milling, and radiation damage all contribute to blurring of the HRTEM images. To reduce the background noise, rotational-filtering was applied to selected digitized HRTEM images using software from Digital Micrograph (Gatan Inc.). In some instances it was useful to observe a given image at a lower resolution than was obtained experimentally. For those cases we generated the Fourier-transform of

the experimental image and calculated the inverse transform to yield an image at the desired resolution. We simulated HRTEM images using the Cerius<sup>2</sup> 3.5 software (Molecular Simulation Institute, Inc.) and atomic positions and thermal parameters listed by Spinnler (1985) for the model of Kunze (1958).

### RESULTS

Except for that of Viti and Mellini (1996), previous TEM investigations of antigorite were based on projections from a single crystallographic orientation. However, this approach risks missing features in three-dimensional crystals. In this study we utilized both [001] and [010] orientations. We consider these two directions in turn.

#### [001] projections

The [001] viewing direction of antigorite provides information about structural details of sheets of coordination polyhedra in the **a-b** plane. However, it can be challenging to find the [001] orientation. The antigorite **c** axis is determined by the layering, which is affected by the structural modulations. We assume that antigorite has a lizardite subcell, consistent with the Kunze model, in which case the (001) plane of the subcell is parallel to that of the supercell. However, we found that  $\mathbf{c}_{\text{subcell}}$  and  $\mathbf{c}_{\text{supercell}}$  are not necessarily parallel.

Most crystals from all three localities are characterized by a  $\sim 35$  Å modulation wavelength, but a few percent of the grains from each sample show different modulation wavelengths and disordering along the **a** axis. The crystals show one of two types of reciprocal lattice geometries: the first type has orthogonal axes (Fig. 2a), whereas in the other the angle between the line of superlattice reflections and any other axis in the  $hk0$  reciprocal plane has a value not equal to  $90^\circ$  (Fig. 2b), resulting in non-orthogonal axes. However, both types of samples are modulated and incommensurate with respect to the subcell. For indexing SAED patterns we assumed *C*-centered subcells and used  $a = 5.44$ ,  $b = 9.23$  Å, and  $\beta, \gamma = 90^\circ$  for both types of samples. We used  $c = 7.27$  Å and  $\alpha = 90^\circ$  for the subcells with orthogonal axes, and  $c = 7.86$  Å and  $\alpha = 113.06^\circ$  for subcells with non-orthogonal axes. These values correspond to those of [001] lizardite-1T (Fig. 2a) and a [001] lizardite polytype having  $b/3$  translations between adjacent layers (Fig. 2b).

The observed [001] antigorite patterns do not match calculated SAED patterns based on the Kunze-Spinnler atomic positions (Fig. 3). In contrast to the experimental patterns, the strong subcell reflections have nearly uniform intensities in the calculated pattern. In spite of the absence of 010 subcell reflections in the experimental patterns, there are relatively strong superlattice reflections at their positions (indicated by arrows) in Figure 3. The main characteristic of the calculated  $hk0$  supercell reflections is that their intensity distributions parallel to  $\mathbf{a}^*$  in  $k = 2n$  and  $k = 2n + 1$  rows are different. The  $k = 2n$

**TABLE 1.** Compositions of the antigorite samples from analytical electron microscopy

Locality	Si at%	Mg at%	Al at%	Fe at%	Formula
Felsőcsatár	38.71 (0.91)	50.57 (1.21)	5.57 (0.32)	5.15 (0.22)	$(\text{Mg}_{42}\text{Fe}_{2}^{2+}\text{Al}_2)[\text{Si}_{32}\text{Al}_2\text{O}_{85}(\text{OH})_{62}]$
Val Antigorio	38.50 (0.87)	51.15 (1.19)	6.35 (0.34)	4.26 (0.20)	$(\text{Mg}_{42}\text{Fe}_{3}^{2+}\text{Fe}^{3+}\text{Al}_2)[\text{Si}_{31}\text{Al}_3\text{O}_{85}(\text{OH})_{62}]$
Deligh Quarry	39.64 (0.90)	53.68 (1.17)	4.24 (0.27)	2.73 (0.15)	$(\text{Mg}_{44}\text{Fe}_{2}^{2+}\text{Al}_2)[\text{Si}_{32}\text{Al}_2\text{O}_{85}(\text{OH})_{62}]$

*Note:* The compositions are averages of five analyses. The cation contents are normalized to 100%. The values of  $2\sigma$  (where  $\sigma = n^{1/2}/n$ ,  $n$  = number of counts) are given in parentheses. Formulas are expressed in the  $\text{M}_{48}^{2+}[\text{T}_{34}\text{O}_{85}(\text{OH})_{62}]$  general form of antigorite.

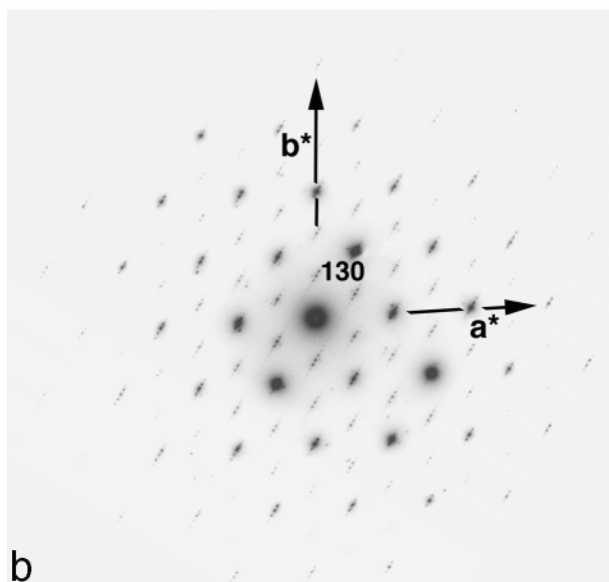
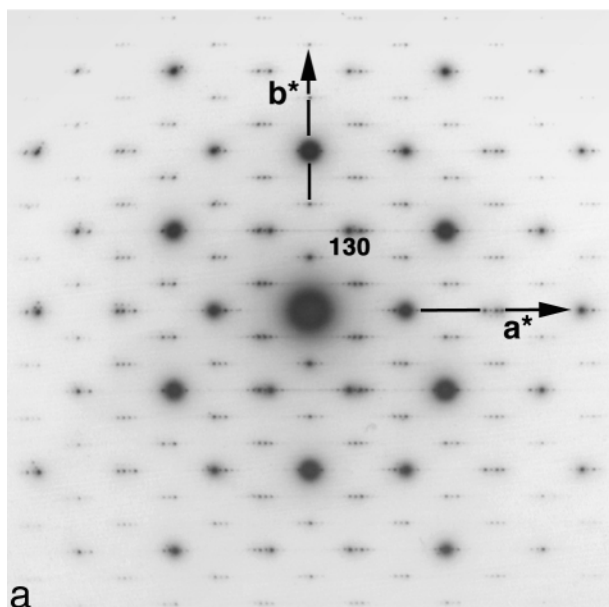


**FIGURE 2.** (a) [001] SAED pattern of an antigorite crystal (Felsőcsatár). (b) SAED pattern of an antigorite crystal in a projection with a high angle to the  $a$ - $b$  plane. The rows of superlattice reflections, defined by multiple spots, are parallel to the  $[130]^*$  direction referred to the subcell (Val Antigorite).

rows contain relatively few reflections, all of which are weak. The  $k = 3$  row contains fewer reflections than the  $k = 1$  row. The superlattice reflections in the experimental SAED patterns do not show these intensity differences.

Simulated [001] HRTEM images based on the Kunze model are shown as a function of objective-lens defocus in Figures 4c to 4t at 2 and 3 Å resolutions and a sample thickness of 131 Å. Each of these figures shows an area of six unit cells ( $2a \times 3b$ ). The contrast in all images is dominated by the superimposed Si-O positions of the T sheets (the dark spots in the image of projected potential in Fig. 4b). The alternating four- and eight-

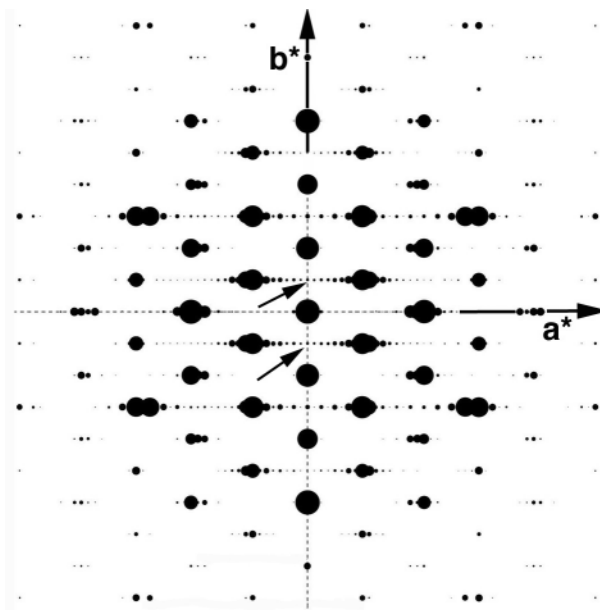


**FIGURE 3.** Calculated [001] SAED pattern of antigorite based on the Kunze (1958) model. Note the similarity of the geometry, but not the intensity distribution, to Figure 2a. Small arrows point to 010 reflections.

membered rings aligned parallel to  $[010]$  in the tetrahedral sheets are recognizable in every image. However, the inversions in the tetrahedral sheets at the  $2_1$  axes are not evident in the simulated HRTEM images, even at the conditions that were used to create Figures 4g,h and 4p,q (near to the Scherzer-defocus value).

Figure 5a is an experimental [001] HRTEM image of the crystal whose diffraction pattern is shown in Figure 2b. The modulation wavelength is  $\sim 35$  Å. The Fourier-transform of this image (Fig. 5c) matches Figure 2b. Figure 5b demonstrates the effects of rotational filtering. The filtered image is free of artifacts and the noise was reduced significantly.

Comparison of the experimental and simulated HRTEM images indicates that Figure 5 cannot be properly interpreted on the basis of the Kunze model. No reasonable match was found between images in Figures 4 and 5. There are significant differences between them, particularly at the places of inversions in the tetrahedral sheets. The four- and eight-membered rings, if they existed, would require antiphase-like offsets in the  $\{110\}$  subcell planes. Such offsets are evident in the enlarged (Fig. 6) simulated image of Figure 4g, but not in the experimental micrographs (Fig. 5).

There is also no satisfactory match between simulated and experimental HRTEM images for antigorite crystals showing orthogonal axes. The HRTEM image of the antigorite crystal (Fig. 7) corresponding to the SAED pattern in Figure 2a was obtained using a larger objective aperture than for the image in Figure 5, resulting in higher resolution. A diffraction pattern calculated from the experimental image (inserted at the upper left in Fig. 7) indicates a resolution of  $\sim 1.6$  Å and matches the experimental SAED pattern. This antigorite image also differs

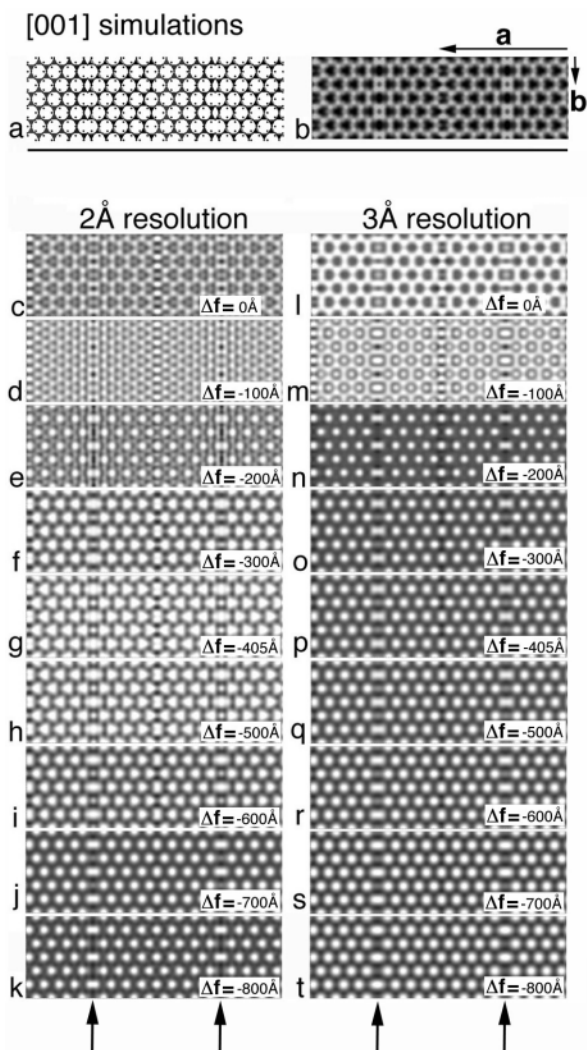


FIGURE 4. (a) [001] view of the Kunze (1958) model of antigorite. (b) [001] projected charge density of antigorite calculated using structural data from the Kunze model with atom coordinates generated by Spinnler (1985). (c to k) and (l to t) Defocus ( $\Delta f$ ) series of simulated HRTEM images of antigorite at 2 and 3 Å resolutions, respectively. Note that all of the images show four- and eight-membered rings (separated from one another by one translation unit, i.e., =  $a_0$ ).

FIGURE 5. (a) [001] HRTEM image of an antigorite crystal from Val Antigorio; it shows different contrast from that in any of the simulated images in

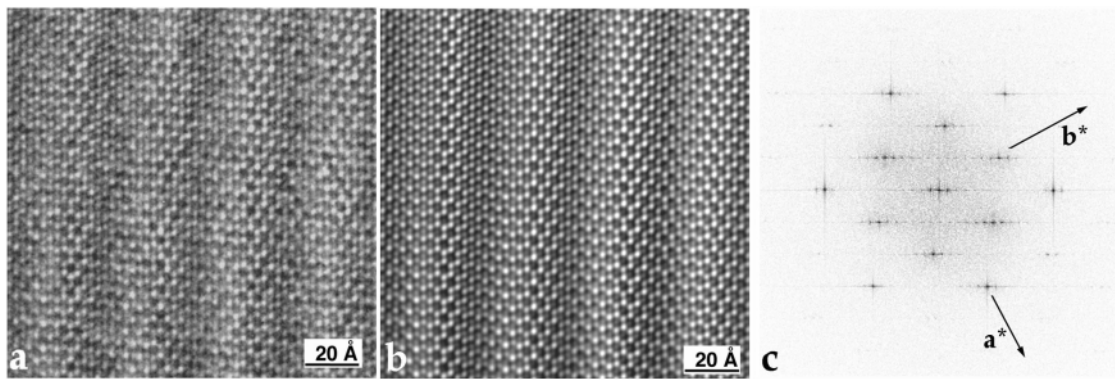


Figure 4. The SAED pattern of this crystal is shown in Figure 2b. (b) Corresponding rotationally filtered HRTEM image. (c) Calculated diffraction pattern of the experimental image in a.

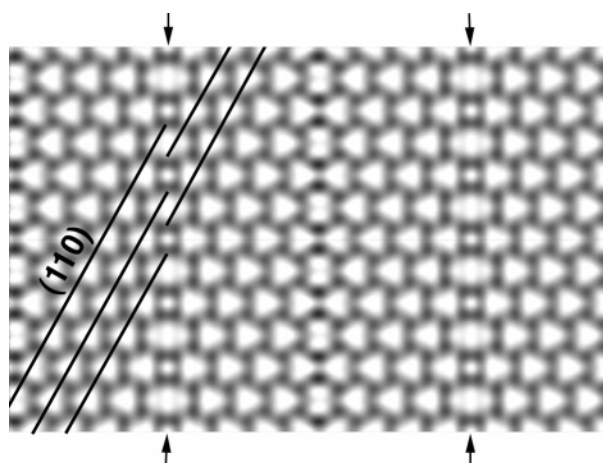


FIGURE 6. Antiphase-like offsets in the (110) planes (black lines) of the subcell at a [010] row of four- and eight-membered rings (marked by arrows) in an image simulated at Scherzer defocus for the Kunze model. Identical offsets occur along  $(\bar{1}\bar{1}0)$ . This image corresponds to Figure 4g but at higher magnification.

from the simulated images that were calculated from the Kunze model. Neither the original experimental HRTEM images nor the reduced-resolution images show the four- and eight-membered rings and the offsets in the subcell {110} planes.

#### [010] projections

[010] is the most commonly studied projection of antigorite (Yada 1979; Spinnler 1985; Mellini et al. 1987; Otten 1993). It provides information about the modulation profile, the relative positions of the T and O cations, and the stacking of the 1:1 layers.

No ordered subcell reflections are apparent in the calculated [010] SAED pattern for the Kunze model (Fig. 8). Most of the strong reflections lie off the lines parallel to  $c^*$ , along which  $h0l_{\text{subcell}}$  reflections would be expected to occur. Only a few weak superlattice reflections appear along the  $c^*$  axis. The  $h00$  row is practically free of superlattice reflections, consistent with the calculated [001] SAED pattern (Fig. 3).

Several significant features in the experimental [010] SAED

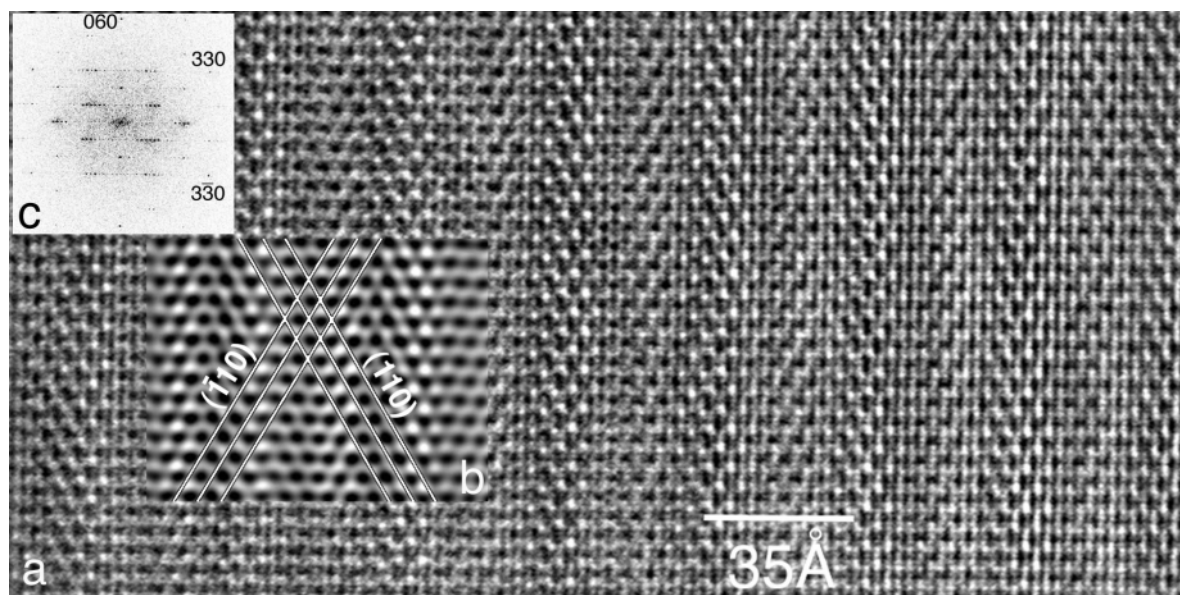


FIGURE 7. (a) [001] HRTEM image of an antigorite crystal (Felsőcsatár). There is no good match between this and the simulated images in Figure 4. The SAED pattern of this crystal is shown in Figure 2a. (b) For improved viewing of the {110} fringes, the resolution of the experimental image was reduced to 3 Å by Fourier-filtering, as shown in the boxed part of the image. There are no traces of offsets in the {110} planes (white lines). (c) Diffraction pattern calculated from the HRTEM image, showing the 060 and 330 reflections and that structural details down to a resolution of 1.5 Å are visible in the experimental image.

patterns (e.g., Fig. 9) differ from those of the calculated pattern: (1) all experimental patterns contain far more superlattice reflections, (2) the most intense superlattice reflections occur along the  $h00$  row, (3) the strong reflections are ordered along both  $c^*$  and  $a^*$ , and (4)  $\beta = 90^\circ$ . The streaks parallel to  $c^*$  indicate (001) faults.

There is a one-to-one correspondence between the cation positions in the Kunze model and the dark spots in the calculated HRTEM images (Fig. 10). The images, as can be seen by the light interlayer regions, shift slightly as a function of defocus between  $-200$  and  $0$  Å (Figs. 10c–e). The wavy lines of the O positions are continuous, whereas the lines of the T positions are broken at inversions for defocus values from  $-300$  to  $-800$  Å (Figs. 10f–k).

Important chemical details of antigorite are measurable using [010] HRTEM images. Antigorite differs from lizardite and chrysotile by a slight deficiency in octahedral cations and hydroxyls. As the simulated images demonstrate, we can determine the local compositions from image details. Based on the number of dots corresponding to the T and O positions within a period, we can deduce the actual formula. In [010] projections, the dark spots at T positions represent the  $[\text{Si}_2\text{O}_5(\text{OH})]^{3-}$  chemical unit of the T sheet, whereas spots at O positions correspond to  $[\text{Mg}_3(\text{OH})_3]^{3+}$ . However, a special situation exists for the O sites that lie on (100) planes near the origin (short arrows in Fig. 1). The atoms in three O sites within the (100) planes and aligned along [010] occupy special positions. They are coordinated to the two adjacent  $[\text{Si}_2\text{O}_5(\text{OH})]^{3-}$  units. When viewed down [010] these three sites lie above one another so that they, like all the other Mg sites, project as one spot. There is one such special site per repeat period along  $a$ , and it corre-

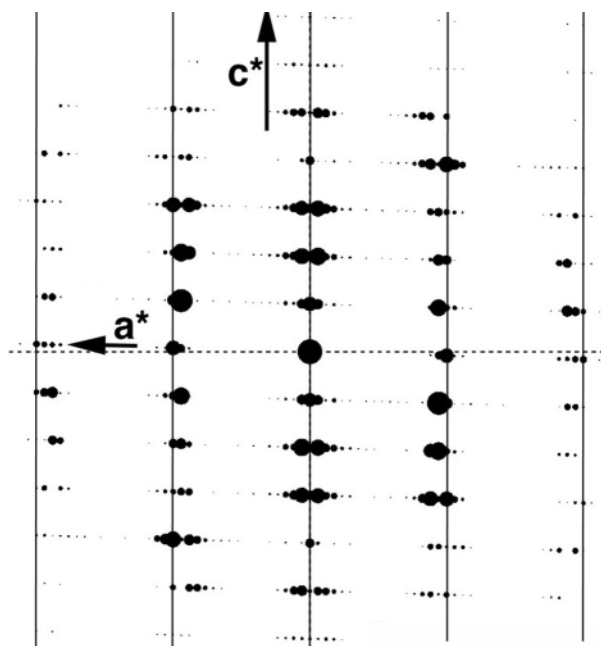


FIGURE 8. Calculated [010] SAED pattern for the Kunze (1958) model. The vertical lines mark the positions of  $h0l$  subcell reflections. Most strong antigorite reflections lie off these lines.

sponds to  $3\text{Mg}^{2+}$  per unit cell. If  $n\text{T}$  and  $m\text{O}$  dots occur within a period in an [010] HRTEM image, the composition can be deduced as  $\text{Mg}_{3m}[\text{Si}_{2n}\text{O}_{5n}(\text{OH})_{n+3(m-1)}]$ . For the Kunze model  $n = 17$  and  $m = 16$  (Fig. 10), so the composition is

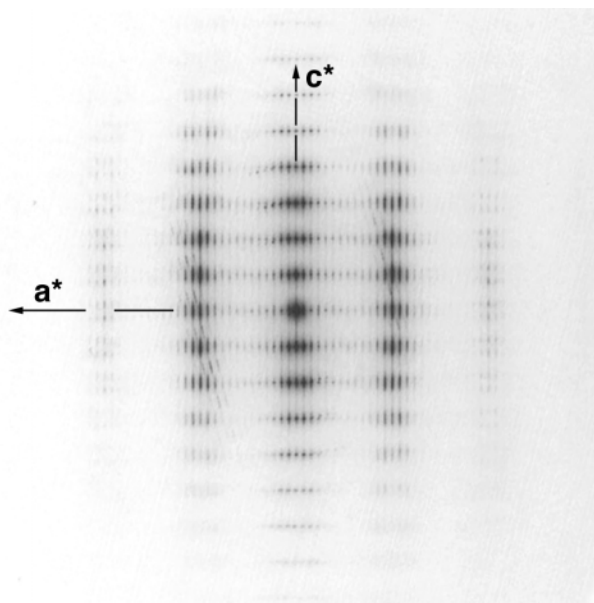


FIGURE 9. [010] SAED pattern of antigorite (Deligh quarry).

[010] simulations

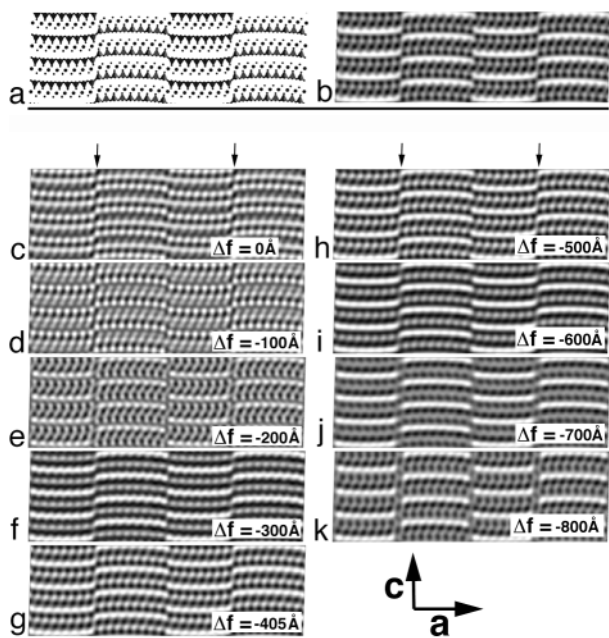


FIGURE 10. (a) [010] view of the Kunze (1958) model of antigorite. (b) Projected charge density, and (c-k) simulated 2 Å resolution HRTEM images using the same data set as for Figure 4. Figure 10g is calculated at Scherzer defocus (-405 Å). The sample thickness is 111.6 Å. Arrows mark the rows of four- and eight-membered rings in the T sheet.

FIGURE 11. (a) Experimental [010] HRTEM images of the Deligh quarry  $n = 14$  antigorite crystal for which a SAED pattern is shown in Figure 9. (b) Rotationally filtered image of (a). (c) Fourier filtered image of (a). The insert in (c) is an enlarged portion of the marked area in (b). The T and O positions are marked within a period (boxed); there are 14 T and 13 O positions.

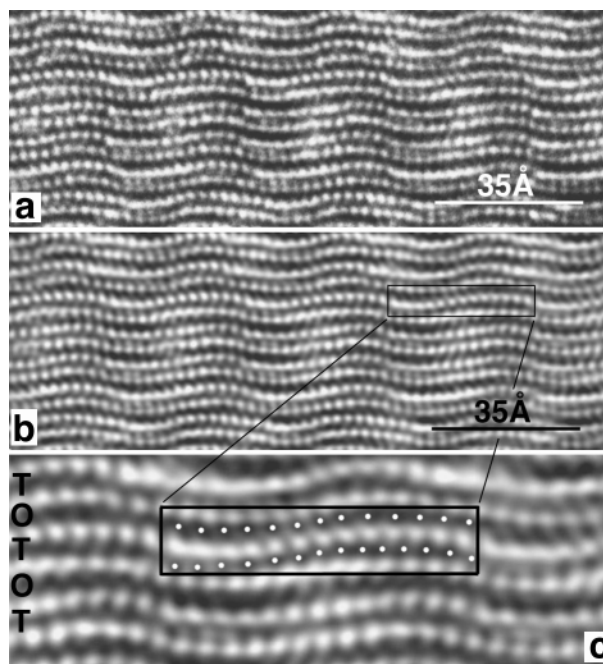


The main structural feature of antigorite is the modulation. The curvature of the modulation half-waves is proportional to the degree of lateral misfit between adjacent T and O sheets. The radius of the half-waves as defined by the octahedral positions in simulated images is 74 Å. This value is the same as obtained by geometrical calculations based on the O atom coordinates listed by Spinnler (1985). In contrast to the results of Spinnler (1985), we found that the curvatures of half-waves in simulated HRTEM images do not vary with sample thickness and focusing conditions. Thus, in experimental HRTEM images the observed curvatures of the O sheets can be used to determine the radius of the half-waves.

We measured structural features of antigorite in experimental HRTEM images and compared them to the simulated ones. The images in Figure 11 and the SAED pattern in Figure 9 were obtained from the same crystal. The resolution allows us to observe the projected cation positions (Fig. 11c). The numbers of T and O positions within a period are 14 and 13, respectively, so the deduced formula of this antigorite sample is  $Mg_{39}[Si_{28}O_{70}(OH)_{50}]$ . The radius of the half-wave was determined from measurements of the wavelength (35 Å) and amplitude (2.18 Å) in Figure 11c by assuming that it can be approximated as a section of a cylinder. The results are 36 Å for the radius and 28.4° for the subtended angle of the half-wave arc.

New structure models for antigorite

The following models, which retain the half-wave character and tetrahedral inversions proposed by Kunze (1958), no longer contain the four- and eight-membered rings in the tetrahedral layers and so are consistent with our HRTEM results. We base our models on the lizardite structure for the orthogonal subcell of antigorite. We use subcell parameters of  $a = 5.44$ ,



$b = 9.2318$ , and  $c = 7.27$  Å, where  $b$  and  $c$  are from Spinnler (1985) and  $a$  is the mean subcell value deduced from the antigorite supercell periodicities given by Wicks and O'Hanley (1988), after Uehara and Shirozu (1985). The  $x$  and  $y$  atomic coordinates for lizardite are from Mellini (1982), and the  $z$  coordinates were deduced from the published thicknesses of structural sheets of antigorite (Wicks and O'Hanley 1988).

To generate the antigorite modulations, we used a model in which a lizardite layer is curled into a cylinder, with the cylinder axis parallel to  $[010]_{\text{liz}}$ . For an antigorite modulation, the expression for the radius of curvature,  $R$ , of a half-wave of the modulation is:

$$2\pi R \cdot \frac{\alpha}{360} = 2\pi(R+d) \cdot \frac{\alpha}{360} \cdot \frac{m}{n}$$

where the left side of the equation represents the length of the arc ( $na/4$  Å) in the  $a$  direction formed by the O atoms in the basal plane of the  $\text{SiO}_4$  tetrahedra. The right side represents the length of the parallel arc along the Mg sites in the octahedral sheet;  $\alpha$  is the subtended angle of the arc, and  $d$  is the separation (2.885 Å) of the octahedral and tetrahedral planes. Finally,  $R = md$ , and  $n = 45a/md$ , where  $m$  and  $n$  are the numbers of projected O and T cation sites in these two sheets per unit cell (Fig. 12). The result of these calculations for our case ( $m = 13$  and  $n = 14$ ) is a radius of 37.5 Å and a subtended angle of  $29^\circ$ . These values are similar to the measured values of 36 Å and  $28.4^\circ$ . The resulting chord length of the arc for a half-wave is 17.5 Å, which is half the observed 35 Å wavelength of modulation. The atomic coordinates of the resulting antigorite structure are listed in Table 2.

The full-wave modulation can be generated by reversing the half-wave by operation of a  $2_1$  screw axis oriented parallel to  $[010]$  and located at the position marked by an asterisk (arrowed) in Figure 12. For these geometrical conditions, the rotated octahedra form a continuous sheet across the positions at which the T sheets reverse orientation. The resulting unit cell has orthogonal axes and a stoichiometry that matches the deduced  $\text{Mg}_{39}[\text{Si}_{28}\text{O}_{70}(\text{OH})_{50}]$  composition from HRTEM images. Analogous calculations can be made for antigorite crystals having any given modulation wavelength.

### Comparisons with previous models

Differences among the antigorite models of Kunze (1958), Uehara and Shirozu (1985), and ours lie in the presence or absence of four- and eight-membered rings and offsets, relative to lizardite, within the Mg and (OH) planes (marked by  $\uparrow\downarrow$  in Fig. 13). According to Kunze (1958), the tetrahedral sheets contain one four- and one eight-membered ring per supercell (Fig. 13a). The offsets [along (100) with displacement  $b/2$ ] bisect these sets of four- and eight-membered rings and, additionally, lie midway between them at the positions of the inversions of the tetrahedral sheets. The O coordinations along offsets differ near the positions of the  $2$  and  $2_1$  rotation axes in the T sheet (Fig. 14). At the twofold axis the (100) displacement plane is located between the  $[010]$  rows of octahedral cations, and the nearest O atom neighbors form a tetragonal pyramid around the Mg positions (Fig. 14a); the Mg atoms are located at the bases of the coordination

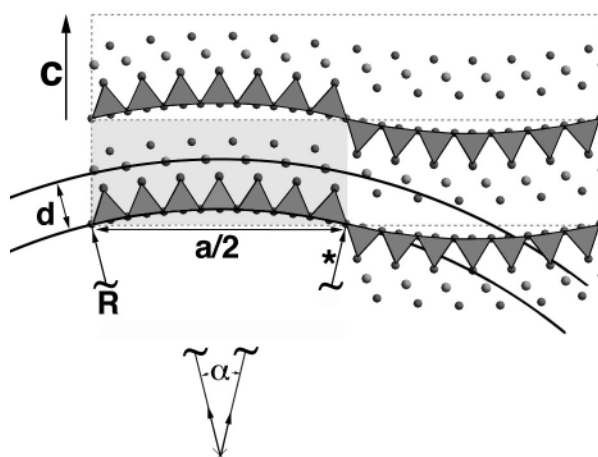


**FIGURE 12.** Generation from lizardite of a modulated antigorite with 14 T positions in a wavelength. The basal plane of the T sheet is curled onto a cylinder with the radius,  $R$ , of the half-wave curvature. The value of  $R$  is determined by the distance,  $d$ , between the basal plane of the tetrahedra and the plane of the centers of octahedral cations, and by the numbers of T and O positions (7 and 6.5) along an arc having a chord length of a half period of the modulation  $a/2$ . The arrow at the asterisk points to the axis of reversal. The interrelations of  $d$ ,  $a$ , and  $R$  are given in the text.

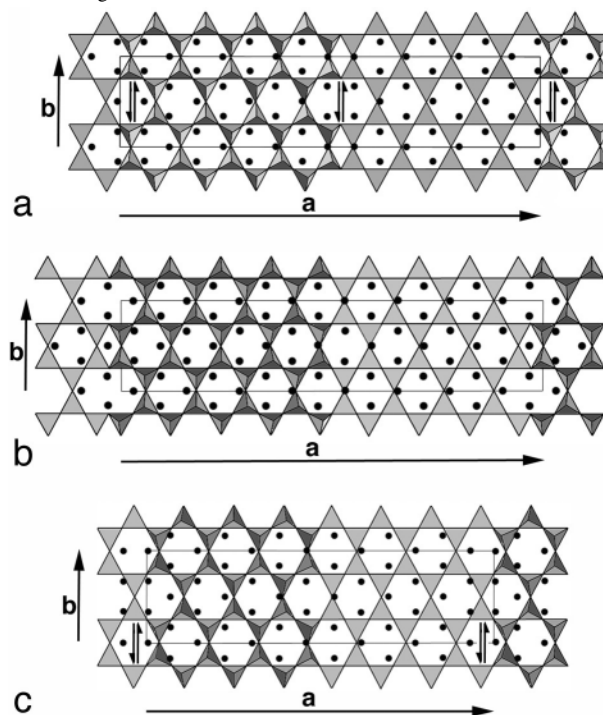


**FIGURE 13.** Antigorite structure models viewed perpendicular to the TO layers. (a) Kunze (1958) model for  $n = 17$  antigorite. There are two offsets in the O sheet (marked by  $\uparrow\downarrow$ ) and four- and eight-membered rings in the T sheet in the middle of the unit cell. (b) Model of Uehara and Shirozu (1985) for  $n = 17$  antigorite. There is no offset in the O sheet. The four- and eight-membered rings in the T sheet are shifted with  $a/2$  compared to the Kunze model. (c) Our model for  $n = 14$  antigorite. There are no four- and eight-membered rings in the T sheet. The number of offsets in the O sheet is half that in the Kunze model.

TABLE 2. Atomic coordinates for antigorite-*M* with  $n=14$ 

	<i>x</i>	<i>y</i>	<i>z</i>		<i>x</i>	<i>y</i>	<i>z</i>
Mg 1	0.06768	0.50000	0.56156	O 23	0.17443	0.16667	0.44803
Mg 2	0.00468	0.00000	0.52401	O 24	0.14205	0.24565	0.13156
Mg 3	0.06783	0.83365	0.56167	O 25	0.39585	0.50000	0.11059
Mg 4	0.00482	0.33365	0.52417	O 26	0.32412	0.00000	0.14605
Mg 5	0.22438	0.50000	0.62958	O 27	0.43892	0.50000	0.72800
Mg 6	0.14579	0.00000	0.60828	O 28	0.35848	0.00000	0.77602
Mg 7	0.22452	0.83365	0.62960	O 29	0.32712	0.50000	0.45681
Mg 8	0.14594	0.33365	0.60835	O 30	0.40318	0.00000	0.41967
Mg 9	0.38155	0.50000	0.59563	O 31	0.35803	0.74565	0.13222
Mg 10	0.30308	0.00000	0.62536	O 32	0.35877	0.66730	0.77589
Mg 11	0.38170	0.83365	0.59555	O 33	0.43921	0.16730	0.72777
Mg 12	0.30323	0.33365	0.62533	O 34	0.40293	0.66667	0.41095
Mg 13	0.45942	0.00000	0.54054	O 35	0.32700	0.16667	0.44803
Mg 14	0.45957	0.33365	0.54041	O 36	0.28609	0.24565	0.15537
Mg 15	0.93232	0.00000	0.47145	O 37	0.46691	0.00000	0.05196
Mg 16	0.93217	0.33365	0.47134	O 38	0.47854	0.50000	0.35797
Mg 17	0.77562	0.00000	0.40343	O 39	0.47818	0.16667	0.34935
Mg 18	0.85421	0.50000	0.42473	O 40	0.42948	0.24565	0.08580
Mg 19	0.77548	0.33365	0.40341	O 41	0.89174	0.00000	-0.07933
Mg 20	0.85406	0.83365	0.42466	O 42	0.96284	0.50000	-0.02156
Mg 21	0.61845	0.00000	0.43738	O 43	0.88433	0.00000	0.27031
Mg 22	0.69692	0.50000	0.40765	O 44	0.96452	0.50000	0.32715
Mg 23	0.61830	0.33365	0.43746	O 45	0.97712	0.00000	0.67505
Mg 24	0.69677	0.83365	0.40768	O 46	0.90175	0.50000	0.61334
Mg 25	0.54058	0.50000	0.49247	O 47	0.92939	0.24565	-0.05169
Mg 26	0.54043	0.83365	0.49260	O 48	0.96423	0.16730	0.32689
Si 1	0.10469	0.66667	0.19094	O 49	0.88403	0.66730	0.27015
Si 2	0.03250	0.16667	0.13184	O 50	0.90150	0.16667	-0.37794
Si 3	0.39674	0.66667	0.19094	O 51	0.97675	0.66667	-0.31633
Si 4	0.32389	0.16667	0.22651	O 52	0.74793	0.00000	-0.12517
Si 5	0.25071	0.66667	0.23838	O 53	0.82000	0.50000	-0.11392
Si 6	0.17753	0.16667	0.22651	O 54	0.72246	0.00000	0.23515
Si 7	0.89531	0.16667	-0.15793	O 55	0.80351	0.50000	0.23960
Si 8	0.96750	0.66667	-0.09883	O 56	0.82569	0.00000	0.57620
Si 9	0.46893	0.16667	0.13184	O 57	0.74929	0.50000	0.56380
Si 10	0.74929	0.16667	-0.20537	O 58	0.78601	0.24565	-0.12214
Si 11	0.82247	0.66667	-0.19350	O 59	0.80322	0.16730	0.23953
Si 12	0.60326	0.16667	-0.15793	O 60	0.72216	0.66730	0.23518
Si 13	0.67611	0.66667	-0.19350	O 61	0.74929	0.16667	-0.42740
Si 14	0.53107	0.66667	-0.09883	O 62	0.82557	0.66667	-0.41502
O 1	0.10826	0.50000	0.11234	O 63	0.85795	0.74565	-0.09855
O 2	0.03716	0.00000	0.05458	O 64	0.60415	0.00000	-0.07758
O 3	0.11567	0.50000	0.76270	O 65	0.67588	0.50000	-0.11304
O 4	0.03548	0.00000	0.70587	O 66	0.56108	0.00000	0.30502
O 5	0.02288	0.50000	0.35797	O 67	0.64152	0.50000	0.25699
O 6	0.09825	0.00000	0.41967	O 68	0.67288	0.00000	0.57620
O 7	0.07061	0.74565	0.08471	O 69	0.59682	0.50000	0.61334
O 8	0.03577	0.66730	0.70612	O 70	0.64197	0.24565	-0.09920
O 9	0.11597	0.16730	0.76286	O 71	0.64123	0.16730	0.25712
O 10	0.09850	0.66667	0.41095	O 72	0.56079	0.66730	0.30524
O 11	0.02325	0.16667	0.34935	O 73	0.59707	0.16667	-0.37794
O 12	-0.00001	0.24565	0.01480	O 74	0.67300	0.66667	-0.41502
O 13	0.25207	0.50000	0.15818	O 75	0.71391	0.74565	-0.12236
O 14	0.18000	0.00000	0.14693	O 76	0.53309	0.50000	-0.01895
O 15	0.27754	0.50000	0.79786	O 77	0.52146	0.00000	0.67505
O 16	0.19649	0.00000	0.79341	O 78	0.52182	0.66667	-0.31633
O 17	0.17431	0.50000	0.45681	O 79	0.57052	0.74565	-0.05278
O 18	0.25071	0.00000	0.46921	O 80	0.49988	0.24565	0.01669
O 19	0.21399	0.74565	0.15515				
O 20	0.19678	0.66730	0.79348				
O 21	0.27784	0.16730	0.79783				
O 22	0.25071	0.66667	0.46041				

Note: The hydrogen positions are omitted. Space group: *Pm*,  $a = 35.02$ ,  $b = 9.23$ ,  $c = 7.27$  Å, and  $\beta = 90^\circ$ . The significance of the bold atoms is explained in the text

pyramids. At the  $2_1$  axis the coordination polyhedron of the Mg atoms changes from an octahedron to a three-sided prism (shaded in Fig. 14b).

Relative to Kunze (1958), Uehara and Shirozu (1985) moved the origin of the antigorite unit cell by  $(a + b)/2$  (Fig. 13b). This shift leaves the T sheets identical to the model of Kunze but produces continuous octahedral sheets, as in lizardite, but

without the offsets of the Kunze model.

Our model differs from both of the above (Fig. 13c) in that we find no need for the four- and eight-membered rings, and all the rings have roughly the hexagonal configurations typical of layer silicates. Moreover, compared to the Kunze model, ours has half the number of offsets in the octahedral sheets. The coordination number of the Mg atoms along these offsets is six, and the O atoms form three-sided prisms (Fig. 14b), as they do in the Kunze model.

The modulation lengths of the antigorite samples ranges from 33 Å (Mellini and Zussman 1986) to 110 Å (Chapman and Zussman 1959). The range results from differences in the number of tetrahedra in a period. However, a distinction needs to be made between crystals having even and odd numbers of tetrahedra in a period. The model described above applies to the former case, with a supercell having orthogonal axes (although its symmetry is monoclinic, with space group *Pm*).

Phyllosilicates such as chlorite- and lizardite-group minerals can exhibit displacements of adjacent layers by  $b/3$  and  $a/3$  and their symmetry equivalents. Such displacements result in polytypism if the displacements are periodic. Antigorite can display similar layer displacements, except that the modulations constrain the structure so that only  $\pm b/3$  displacements can occur. Atomic coordinates for a model antigorite structure having 14 tetrahedra in a period with  $b/3$  displacements between adjacent layers (Fig. 15) are given in Table 3.

In contrast, many antigorite samples contain eight and nine tetrahedra in the two adjacent half-waves of a period (Kunze 1958; Uehara and Shirozu 1985; Spinnler 1985; Mellini et al. 1987; Wicks and O'Hanley 1988; Otten 1993), such that the modulation wavelength is asymmetric, with a pe-

riod of 43.3 Å. In this and all other cases with odd numbers of T positions in a period (Fig. 16), the symmetry is triclinic (space group *P1*). However, the structural principles are the same as for an antigorite having even numbers of tetrahedra. Calculated atomic coordinates for a model antigorite structure with eight and nine tetrahedra ( $n = 17$ ) in one modulation length are given in Table 4.

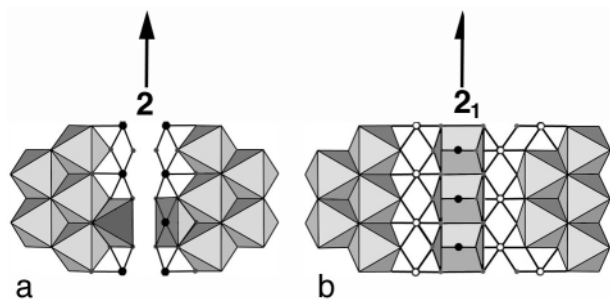


**FIGURE 14.** Coordinations of O positions at the two types of offsets in the Kunze model. They are located in Figure 1 at the 2 and  $2_1$  axes, respectively. (a) The nearest O atom neighbors form a tetragonal pyramid (one is shaded) around the O positions (black dots) at the twofold axis. (b) At the  $2_1$  axis the coordination polyhedron of the O atoms (black dots) changes from an octahedron to a three-sided prism.

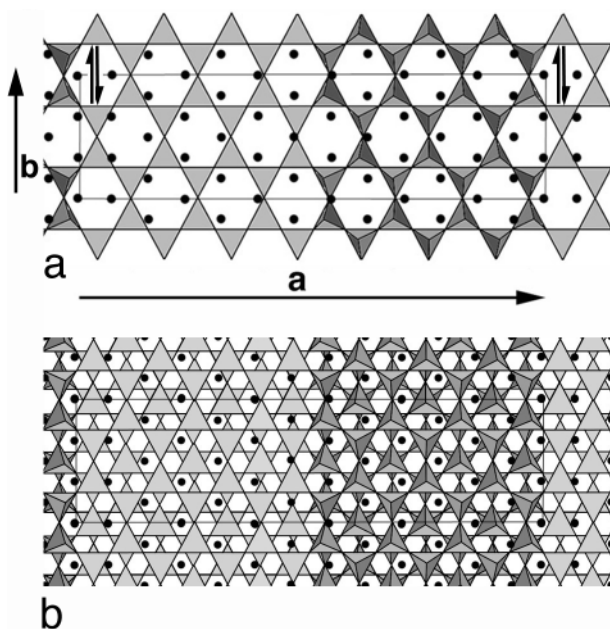


**FIGURE 15.** (a) A single layer of antigorite ( $n = 14$ ) viewed perpendicular to the layer. (b) The same view of antigorite-*T* in which  $b/3$  displacements exist between adjacent layers. The offsets are marked by  $\uparrow\downarrow$  and the unit cells by light lines.

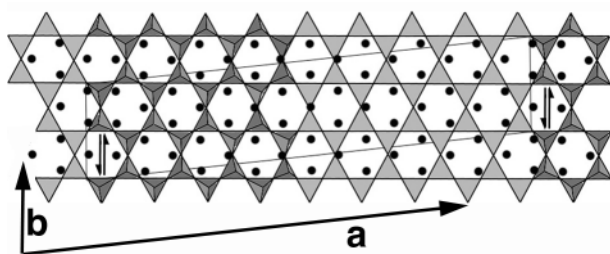


**FIGURE 16.** [001] view of our antigorite-*T* model for  $n = 17$ . There are no four- and eight-membered rings in the T sheet. The offsets in the O sheet are indicated by  $\uparrow\downarrow$ .

### Antigorite-*M* and antigorite-*T*

In the previous sections we demonstrated that the existing antigorite models fail certain critical tests. We proposed alternative models, one for antigorite with orthogonal axes and monoclinic symmetry (antigorite-*M*, Table 2) and the others for antigorite with non-orthogonal axes and triclinic symmetry (antigorite-*T*, Tables 3 and 4). In this section we compare experimental HRTEM images with the corresponding calculated images and use these comparisons as tests of the proposed models.

Provided there are no  $b/3$  displacements between adjoining 1:1 layers, antigorite crystals with even numbers,  $n$ , of T sites parallel to **a** within one modulation wavelength in [010] projections have monoclinic symmetry (antigorite-*M*; Table 2). If the number of T sites is odd when viewed along the same direction, the antigorite has triclinic symmetry (antigorite-*T*; Table 4). If periodic  $b/3$  displacements occur, antigorite also has triclinic symmetry, independent of modulation wavelengths.

All three samples in this study consist mainly of  $n = 14$  varieties, and they are either antigorite-*M* or antigorite-*T*. Figures 17 and 19 to 22 show experimental HRTEM images with superimposed images calculated according to the proposed antigorite structures. Although the overall matches of the geometry are good, there are differences in details. The explanations provide additional insights into the antigorite structure.

Several simplifications were made with the calculated images. We did not correct for (1) thermal parameters for atomic positions, (2) minor atomic displacements within the T and O sheets relative to idealized lizardite, or (3) crystal or beam tilts. These simplifications result in exaggerated differences between the experimental images and the images calculated on the basis of the structure model. However, even considering these differences, the match between the experimental and calculated images is good, which we take to be a confirmation of our proposed model.

The contrast in images perpendicular to the **a-b** plane, or at high angles to that plane, are especially sensitive to TEM focus. It is commonly necessary to tilt the crystals up to  $20^\circ$  to view such projections. For such tilts there will be differences in defocus of  $\sim 100 \text{ \AA}$  between areas of crystals separated by, say,  $300 \text{ \AA}$ . In addition, through-focus series of images were precluded because of the rapid radiation damage of the samples.

The most readily evident conclusion of this study pertains to the four- and eight-membered rings of the Kunze model. Figure 17 shows an antigorite-*M* [001] HRTEM image. The inserted image, which was calculated from our model and does not contain four- and eight-membered rings, matches the experimental image with only minor differences. This result is a confirmation of the model for which the data are given in Table 2.

The proposed model of antigorite-*T* is also free of four- and eight-membered rings. The  $b/3$ -type stacking preserves the value of  $90^\circ$ . A result is that antigorite-*M* and antigorite-*T* have similar [001] SAED patterns. However, the inclined **c** axis in antigorite-*T* presents ambiguities in both SAED patterns and HRTEM images. Several viewing directions produce similar patterns, but only one of them is along [001]. One needs to consider the fine details to discern differences. These other directions are  $[3\bar{1}6]$  and  $[\bar{3}16]$  relative to the subcell (Fig. 18),

TABLE 3. Atomic coordinates for antigorite-*T* with  $n = 14$ 

	<i>x</i>	<i>y</i>	<i>z</i>		<i>x</i>	<i>y</i>	<i>z</i>		<i>x</i>	<i>y</i>	<i>z</i>
Mg 1	0.93232	0.1281	0.43846	Si 26	0.39674	0.88598	0.15795	O 62	0.17443	0.47167	0.41504
<b>Mg 2</b>	0.99532	0.82533	0.47601	Si 27	0.32389	0.39783	0.19352	O 63	0.14205	0.77850	0.09857
Mg 3	0.93217	0.64643	0.43835	Si 28	0.46893	0.36628	0.09885	O 64	0.39585	0.02586	0.07760
<b>Mg 4</b>	0.99518	0.15893	0.47585	O 1	0.89174	0.46255	0.88768	O 65	0.32412	0.53768	0.11306
Mg 5	0.77562	0.29014	0.37044	O 2	0.96284	0.98181	0.94544	O 66	0.43892	0.89833	0.69500
Mg 6	0.85421	0.79724	0.39174	O 3	0.88433	0.24577	0.23732	O 67	0.35848	0.41434	0.74303
Mg 7	0.77548	0.62378	0.37042	O 4	0.96452	0.76471	0.29415	O 68	0.32712	0.80793	0.42382
Mg 8	0.85406	0.13087	0.39167	O 5	0.97712	0.38068	0.64205	O 69	0.40318	0.29555	0.38668
Mg 9	0.61845	0.30146	0.40439	O 6	0.90175	0.86011	0.58035	O 70	0.35803	0.27872	0.09922
Mg 10	0.69692	0.79155	0.37466	O 7	0.92939	0.71741	0.91531	O 71	0.35877	0.08159	0.74290
Mg 11	0.61830	0.63513	0.40447	O 8	0.96423	0.43193	0.29390	O 72	0.43921	0.56555	0.69478
Mg 12	0.69677	0.12521	0.37469	O 9	0.88403	0.91301	0.23716	O 73	0.40293	0.95931	0.37796
Mg 13	0.54058	0.81982	0.45948	O 10	0.90150	0.52968	0.58907	O 74	0.32700	0.47167	0.41504
Mg 14	0.54043	0.15351	0.45961	O 11	0.97675	0.05022	0.65067	O 75	0.28609	0.78644	0.12238
<b>Mg 15</b>	0.06768	0.84285	0.52857	O 12	0.00001	0.24072	0.98522	O 76	0.46691	0.50632	0.01897
<b>Mg 16</b>	0.06783	0.17654	0.52868	O 13	0.74793	0.44727	0.84184	O 77	0.47854	0.77499	0.32497
Mg 17	0.22438	0.86552	0.59659	O 14	0.82000	0.95102	0.85309	O 78	0.47818	0.43878	0.31635
Mg 18	0.14579	0.35843	0.57529	O 15	0.72246	0.23405	0.20216	O 79	0.42948	0.76325	0.05280
Mg 19	0.38155	0.85421	0.56264	O 16	0.80351	0.73553	0.20661	O 80	0.50012	0.24009	0.98333
Mg 20	0.30308	0.36412	0.59237	O 17	0.82569	0.34773	0.54321	O 81	0.92939	0.22611	0.91531
Mg 21	0.22452	0.19918	0.59661	O 18	0.74929	0.84360	0.53081	O 82	0.96423	0.09733	0.29390
Mg 22	0.14594	0.69210	0.57536	O 19	0.78601	0.69393	0.84487	O 83	0.88403	0.57841	0.23716
Mg 23	0.38170	0.18783	0.56256	O 20	0.80322	0.40281	0.20654	O 84	0.90150	0.19635	0.58907
Mg 24	0.30323	0.69776	0.59234	O 21	0.72216	0.90136	0.20219	O 85	0.97675	0.71688	0.65067
Mg 25	0.45942	0.33584	0.50755	O 22	0.74929	0.51320	0.53961	O 86	0.00001	0.74942	0.98522
Mg 26	0.45957	0.66945	0.50742	O 23	0.82557	0.01732	0.55199	O 87	0.78601	0.20263	0.84487
Mg 27	0.93217	0.97913	0.43835	O 24	0.85795	0.20180	0.86846	O 88	0.80322	0.06821	0.20654
<b>Mg 28</b>	0.99518	0.49163	0.47585	O 25	0.60415	0.46314	0.88943	O 89	0.72216	0.56676	0.20219
Mg 29	0.77548	0.95648	0.37042	O 26	0.67588	0.95132	0.85397	O 90	0.74929	0.17986	0.53961
Mg 30	0.85406	0.46357	0.39167	O 27	0.56108	0.25733	0.27202	O 91	0.82557	0.68399	0.55199
Mg 31	0.61830	0.96783	0.40447	O 28	0.64152	0.74133	0.22400	O 92	0.85795	0.71050	0.86846
Mg 32	0.69677	0.45791	0.37469	O 29	0.67288	0.34773	0.54321	O 93	0.64197	0.21028	0.86780
Mg 33	0.54043	0.48621	0.45961	O 30	0.59682	0.86011	0.58035	O 94	0.64123	0.07407	0.22413
<b>Mg 34</b>	0.06783	0.50924	0.52868	O 31	0.64197	0.70158	0.86780	O 95	0.56079	0.59011	0.27225
Mg 35	0.22452	0.53188	0.59661	O 32	0.64123	0.40867	0.22413	O 96	0.59707	0.19635	0.58907
Mg 36	0.14594	0.02480	0.57536	O 33	0.56079	0.92471	0.27225	O 97	0.67300	0.68399	0.55199
Mg 37	0.38170	0.52053	0.56256	O 34	0.59707	0.52968	0.58907	O 98	0.71391	0.70256	0.84465
Mg 38	0.30323	0.03046	0.59234	O 35	0.67300	0.01732	0.55199	O 99	0.52182	0.71688	0.65067
Mg 39	0.45957	0.00215	0.50742	O 36	0.71391	0.19386	0.84465	O 100	0.57052	0.72575	0.91422
Si 1	0.89531	0.26969	0.80908	O 37	0.53309	0.98268	0.94806	O 101	0.07061	0.77158	0.05171
Si 2	0.96750	0.12272	0.86818	O 38	0.52146	0.38068	0.64205	O 102	0.03577	0.72374	0.67313
Si 3	0.74929	0.58721	0.76164	O 39	0.52182	0.05022	0.65067	O 103	0.11597	0.24265	0.72987
Si 4	0.82247	0.09116	0.77351	O 40	0.57052	0.21705	0.91422	O 104	0.09850	0.62598	0.37796
Si 5	0.60326	0.60302	0.80908	O 41	0.10826	0.02644	0.07935	O 105	0.02325	0.10545	0.31635
Si 6	0.67611	0.09116	0.77351	O 42	0.03716	0.50719	0.02158	O 106	0.21399	0.79506	0.12216
Si 7	0.53107	0.12272	0.86818	O 43	0.11567	0.90990	0.72971	O 107	0.19678	0.75286	0.76049
Si 8	0.10469	0.21931	0.15795	O 44	0.03548	0.39095	0.67287	O 108	0.27784	0.25431	0.76484
Si 9	0.03250	0.69961	0.09884	O 45	0.02288	0.77499	0.32497	O 109	0.25071	0.64247	0.42742
Si 10	0.25071	0.23513	0.20539	O 46	0.09825	0.29555	0.38668	O 110	0.17443	0.13834	0.41504
Si 11	0.17753	0.73117	0.19352	O 47	0.07061	0.26288	0.05171	O 111	0.14205	0.28720	0.09857
Si 12	0.39674	0.21931	0.15795	O 48	0.03577	0.05834	0.67313	O 112	0.35803	0.78742	0.09922
Si 13	0.32389	0.73117	0.19352	O 49	0.11597	0.57725	0.72987	O 113	0.35877	0.74699	0.74290
Si 14	0.46893	0.69961	0.09885	O 50	0.09850	0.95931	0.37796	O 114	0.43921	0.23095	0.69478
Si 15	0.89531	0.26969	0.80908	O 51	0.02325	0.43878	0.31635	O 115	0.40293	0.62598	0.37796
Si 16	0.96750	0.78939	0.86818	O 52	0.25207	0.04172	0.12519	O 116	0.32700	0.13834	0.41504
Si 17	0.74929	0.25387	0.76164	O 53	0.18000	0.53797	0.11394	O 117	0.28609	0.29514	0.12238
Si 18	0.82247	0.75783	0.77351	O 54	0.27754	0.92162	0.76487	O 118	0.47818	0.10545	0.31635
Si 19	0.60326	0.26969	0.80908	O 55	0.19649	0.42014	0.76042	O 119	0.42948	0.27195	0.05280
Si 20	0.67611	0.75783	0.77351	O 56	0.17431	0.80793	0.42382	O 120	0.50012	0.74879	0.98333
Si 21	0.53107	0.78939	0.86818	O 57	0.25071	0.31207	0.43622				
Si 22	0.10469	0.88598	0.15795	O 58	0.21399	0.28636	0.12216				
Si 23	0.03250	0.36628	0.09885	O 59	0.19678	0.08746	0.76049				
Si 24	0.25071	0.90179	0.20539	O 60	0.27784	0.58891	0.76484				
Si 25	0.17753	0.39783	0.19352	O 61	0.25071	0.97580	0.42742				

Note: The hydrogen positions are omitted. Space group =  $P1$ ;  $a = 35.02$ ,  $b = 9.23$ ,  $c = 7.89$  Å;  $\alpha = 112.94^\circ$ ,  $\beta = 90.00^\circ$ ,  $\gamma = 90.00^\circ$ . The significance of the bold atoms is explained in the text

which correspond to the  $[6\bar{1}3\bar{7}8]$  and  $[\bar{6}1\bar{3}78]$  directions of  $n = 14$  antigorite-*T*. Problems can arise if one is unaware of these subtle differences in diffraction space, because the corresponding HRTEM images differ from one another and can easily lead to misinterpreted structures.

Figure 19 shows  $[001]$  HRTEM images of antigorite-*T* with  $n = 14$ . The contrast of these images differs from that of

antigorite-*M* in Figure 17. We used the structural data in Table 3 for the image calculations. The geometries of the calculated images in Figure 19 (inserts) match the experimental ones. However, although the  $(100)$  planes are obvious in the calculated images, they are more prominent in the experimental ones. We consider this difference between the experimental and calculated images as resulting from the instrumental and crystal-

TABLE 4. Atomic coordinates for antigorite- $T$  with  $n = 17$ 

	$x$	$y$	$z$		$x$	$y$	$z$		$x$	$y$	$z$
Mg 1	0.44287	0.02441	0.32461	Si 31	0.73614	0.21937	0.52409	O 74	0.55040	0.47892	0.37704
Mg 2	0.44297	0.69072	0.32449	Si 32	0.79615	0.68937	0.53996	O 75	0.49071	0.00876	0.45049
Mg 3	0.44297	0.35802	0.32449	Si 33	0.91601	0.96277	0.63704	O 76	0.53159	0.73397	0.71898
Mg 4	0.31936	0.08617	0.43602	Si 34	0.85616	0.49269	0.57765	O 77	0.52142	0.66071	0.11774
Mg 5	0.38143	0.55514	0.39167	O 1	0.00342	0.49847	-0.15486	O 78	0.53159	0.24267	0.71898
Mg 6	0.38153	0.22144	0.39159	O 2	0.00342	0.98977	-0.15486	O 79	0.52142	0.32611	0.11774
Mg 7	0.31946	0.75247	0.43596	O 3	0.39758	0.38039	-0.78634	O 80	0.49104	0.34193	0.45914
Mg 8	0.31946	0.41977	0.43596	O 4	0.45721	0.85058	-0.85971	O 81	0.55066	0.81212	0.35877
Mg 9	0.38153	0.88874	0.39159	O 5	0.44681	0.02245	-0.15926	O 82	0.67295	0.08431	0.30639
Mg 10	0.19403	0.14884	0.45612	O 6	0.38942	0.55114	-0.08828	O 83	0.61175	0.61491	0.33498
Mg 11	0.25684	0.61743	0.45752	O 7	0.42673	0.53248	0.48196	O 84	0.61766	0.44529	0.63848
Mg 12	0.25694	0.28373	0.45750	O 8	0.39795	0.04688	0.22243	O 85	0.67657	0.91583	0.61062
Mg 13	0.19413	0.81514	0.45614	O 9	0.45763	0.51703	0.14898	O 86	0.58428	0.46198	0.05708
Mg 14	0.19413	0.48244	0.45614	O 10	0.47412	0.26292	0.79971	O 87	0.64751	0.93036	0.01978
Mg 15	0.25694	0.95103	0.45750	O 11	0.41666	0.79187	-0.11955	O 88	0.67282	0.41770	0.29758
Mg 16	0.06825	0.21173	0.38470	O 12	0.42693	0.86509	0.48173	O 89	0.61156	0.94834	0.32620
Mg 17	0.13111	0.68030	0.43182	O 13	0.41666	0.28317	-0.11955	O 90	0.58973	0.20490	0.65935
Mg 18	0.13121	0.34660	0.43188	O 14	0.42693	0.19969	0.48173	O 91	0.64844	0.67555	0.62121
Mg 19	0.06836	0.87803	0.38479	O 15	0.45721	0.18391	-0.85971	O 92	0.58408	0.12938	0.05723
Mg 20	0.06836	0.54533	0.38479	O 16	0.39758	0.71372	-0.78634	O 93	0.64731	0.59776	0.01986
Mg 21	0.13121	0.01390	0.43188	O 17	0.27530	0.44154	-0.70696	O 94	0.64844	0.18425	0.62121
Mg 22	0.50548	0.50138	0.27486	O 18	0.33649	0.91094	-0.73555	O 95	0.58973	0.71360	0.65935
Mg 23	0.50538	0.83508	0.27499	O 19	0.33059	0.08056	-0.03905	O 96	0.64731	0.26316	0.01986
Mg 24	0.50538	0.16778	0.27499	O 20	0.27167	0.61002	-0.01119	O 97	0.58408	0.79478	0.05723
Mg 25	0.62899	0.43962	0.16346	O 21	0.36407	0.06382	0.54239	O 98	0.61175	0.28157	0.33498
Mg 26	0.56692	0.97066	0.20780	O 22	0.30083	0.59544	0.57970	O 99	0.67295	0.75097	0.30639
Mg 27	0.56682	0.30436	0.20789	O 23	0.27553	0.10809	0.30189	O 100	0.79618	0.02269	0.31657
Mg 28	0.62889	0.77332	0.16351	O 24	0.33679	0.57746	0.27327	O 101	0.73448	0.55354	0.30025
Mg 29	0.62889	0.10602	0.16351	O 25	0.35851	0.32094	-0.05992	O 102	0.73582	0.38620	0.60437
Mg 30	0.56682	0.63706	0.20789	O 26	0.29981	0.85030	-0.02178	O 103	0.79522	0.85650	0.61975
Mg 31	0.81713	0.17919	0.16759	O 27	0.36427	0.39642	0.54224	O 104	0.77503	0.86660	0.01491
Mg 32	0.87999	0.64776	0.21468	O 28	0.30103	0.92804	0.57962	O 105	0.79618	0.35602	0.30777
Mg 33	0.87999	0.98046	0.21468	O 29	0.29981	0.34160	-0.02178	O 106	0.73441	0.88690	0.29143
Mg 34	0.81713	0.51189	0.16759	O 30	0.35851	0.81224	-0.05992	O 107	0.70755	0.14599	0.60465
Mg 35	0.00494	0.25163	0.37693	O 31	0.30103	0.26264	0.57962	O 108	0.76689	0.61631	0.09792
Mg 36	0.94272	0.78274	0.28460	O 32	0.36427	0.73102	0.54224	O 109	0.77483	0.53400	0.01484
Mg 37	0.94262	0.11644	0.28447	O 33	0.33649	0.24427	-0.73555	O 110	0.76689	0.12501	0.60972
Mg 38	0.00484	0.58533	0.37677	O 34	0.27530	0.77487	-0.70696	O 111	0.70755	0.65469	0.60465
Mg 39	0.00484	0.91803	0.37677	O 35	0.15207	0.50316	-0.71714	O 112	0.77483	0.19940	0.01484
Mg 40	0.94262	0.44914	0.28447	O 36	0.21377	0.97231	-0.70082	O 113	0.73448	0.22020	0.30025
Mg 41	0.75431	0.37695	0.14336	O 37	0.21243	0.13964	-0.00494	O 114	0.79618	0.68935	0.31657
Mg 42	0.69151	0.90836	0.14196	O 38	0.15303	0.66934	-0.02032	O 115	0.91939	0.96107	0.41638
Mg 43	0.69141	0.24206	0.14197	O 39	0.23719	0.12726	0.59377	O 116	0.85787	0.49184	0.35532
Mg 44	0.75421	0.71065	0.14333	O 40	0.17332	0.65920	0.58456	O 117	0.85463	0.32679	0.65672
Mg 45	0.75421	0.04335	0.14333	O 41	0.15217	0.16977	0.29170	O 118	0.91387	0.79717	0.71518
Mg 46	0.69141	0.57476	0.14197	O 42	0.21393	0.63889	0.30804	O 119	0.83896	0.33463	0.04736
Mg 47	0.88009	0.31406	0.21477	O 43	0.24070	0.37985	-0.00522	O 120	0.90277	0.80272	0.10297
Mg 48	0.81723	0.84549	0.16765	O 44	0.18135	0.90953	-0.01029	O 121	0.91953	0.29434	0.40769
Si 1	0.39091	0.38373	-0.00783	O 45	0.23739	0.45986	0.59376	O 122	0.85794	0.82514	0.34656
Si 2	0.44890	0.85473	-0.07920	O 46	0.17352	0.99180	0.58463	O 123	0.82632	0.08660	0.63641
Si 3	0.44890	0.18807	-0.07920	O 47	0.18135	0.40083	-0.01029	O 124	0.88566	0.55692	0.68465
Si 4	0.39091	0.71706	-0.00783	O 48	0.24070	0.87115	-0.00522	O 125	0.83875	0.00203	0.04722
Si 5	0.27196	0.44321	0.06937	O 49	0.17352	0.32640	0.58463	O 126	0.90256	0.47012	0.10276
Si 6	0.33148	0.91345	0.04156	O 50	0.23739	0.79446	0.59376	O 127	0.88566	0.06562	0.68465
Si 7	0.33148	0.24678	0.04156	O 51	0.21377	0.30564	-0.70082	O 128	0.82632	0.59530	0.63641
Si 8	0.27196	0.77654	0.06937	O 52	0.15207	0.83649	-0.71714	O 129	0.90256	0.13552	0.10276
Si 9	0.15209	0.50314	0.05947	O 53	0.02885	0.56477	-0.81695	O 130	0.83875	0.66743	0.04722
Si 10	0.21211	0.97314	0.07534	O 54	0.09038	0.03401	-0.75589	O 131	0.85787	0.15850	0.35532
Si 11	0.21211	0.30647	0.07534	O 55	0.09362	0.19905	-0.05729	O 132	0.91939	0.62774	0.41638
Si 12	0.15209	0.83648	0.05947	O 56	0.03438	0.72867	-0.11575	O 133	0.98058	0.43048	0.49959
Si 13	0.03224	0.56308	-0.03762	O 57	0.10939	0.19116	0.55211	O 134	0.97279	0.26771	0.79497
Si 14	0.09208	0.03315	0.02178	O 58	0.04558	0.72307	0.49650	O 135	0.96628	0.27096	0.18159
Si 15	0.09208	0.36648	0.02178	O 59	0.09041	0.70066	0.25291	O 136	0.98078	0.76371	0.49099
Si 16	0.03224	0.89641	-0.03762	O 60	0.12193	0.43925	-0.03698	O 137	0.94476	0.02738	0.75429
Si 17	0.55734	0.14212	0.60726	O 61	0.06258	0.96892	-0.08522	O 138	0.96608	0.93836	0.18131
Si 18	0.49935	0.67111	0.67863	O 62	0.10959	0.52376	0.55225	O 139	0.94476	0.53608	0.75429
Si 19	0.49935	0.33778	0.67863	O 63	0.04578	0.05567	0.49671	O 140	0.96608	0.60376	0.18131
Si 20	0.55734	0.80878	0.60726	O 64	0.06258	0.46022	-0.08522	O 141	0.98058	0.09715	0.49959
Si 21	0.67629	0.08263	0.53006	O 65	0.12193	0.93055	-0.03698	O 142	0.02885	0.89810	-0.81695
Si 22	0.61677	0.61240	0.55787	O 66	0.04578	0.39027	0.49671	O 143	0.02940	0.23944	0.18618
Si 23	0.61677	0.27906	0.55787	O 67	0.10959	0.85836	0.55225	O 144	0.47417	0.77138	0.79993
Si 24	0.67629	0.74930	0.53006	O 68	0.09038	0.36734	-0.75589	O 145	0.71116	0.39853	0.00571
Si 25	0.85616	0.15936	0.57765	O 69	0.55066	0.14545	0.38577	O 146	0.71095	0.06593	0.00571
Si 26	0.91601	0.62943	0.63704	O 70	0.49104	0.67527	0.45914	O 147	0.71095	0.73133	0.00571
Si 27	0.97552	0.43301	0.71798	O 71	0.50144	0.50340	0.75869				
Si 28	0.97552	0.09968	0.71798	O 72	0.55883	0.97470	0.68771				
Si 29	0.79615	0.02270	0.53996	O 73	0.52162	0.99331	0.11752				
Si 30	0.73614	0.55271	0.52409								

Note: The hydrogen positions are omitted. Space group =  $P1$ ;  $a = 43.50$ ,  $b = 9.23$ ,  $c = 7.27$  Å;  $\alpha = 90.00^\circ$ ,  $\beta = 92.00^\circ$ ,  $\gamma = 84.75^\circ$ .

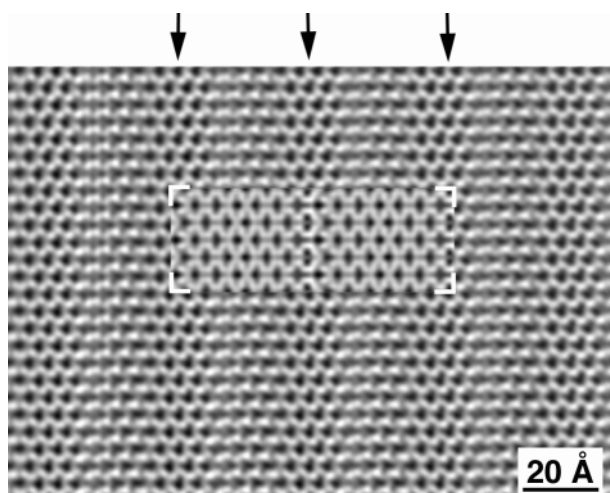


FIGURE 17. [001] HRTEM image of an antigorite-*M* crystal ( $n = 14$ ; Deligh quarry). The resolution of the experimental image, as determined from its calculated diffraction pattern, is 2.2 Å. Minor differences between the experimental and inserted calculated image occur along the [010] direction at the places of offsets (arrowed) in the O sheet. (Sample thickness = 43.6 Å; radius of objective aperture = 0.45 Å<sup>-1</sup>;  $\Delta f = 275$  Å.)

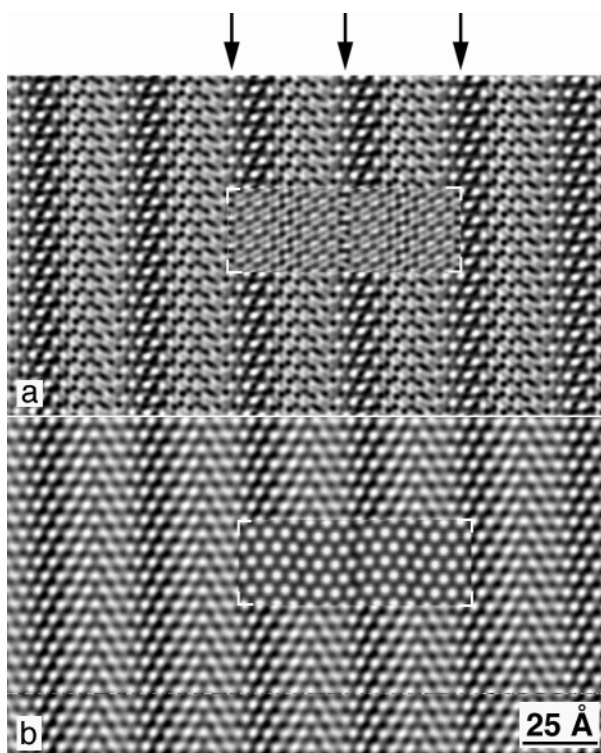


FIGURE 19. (a) [001] HRTEM image of antigorite-*T* ( $n = 14$ ; Deligh quarry). The inserted image was calculated using the coordinates in Table 4 (sample thickness = 95 Å; radius of objective aperture = 0.5 Å<sup>-1</sup>; Scherzer defocus = -405 Å). Minor differences between the experimental and calculated image occur along the [010] direction at the places of offsets (arrowed) in the O sheet. (b) The same image as in (a) but with the resolution reduced to 3 Å through Fourier-filtering. The calculated image (insert) at this lower resolution provides a better match. The absence of the four- and eight-membered rings of the Kunze model is more evident.

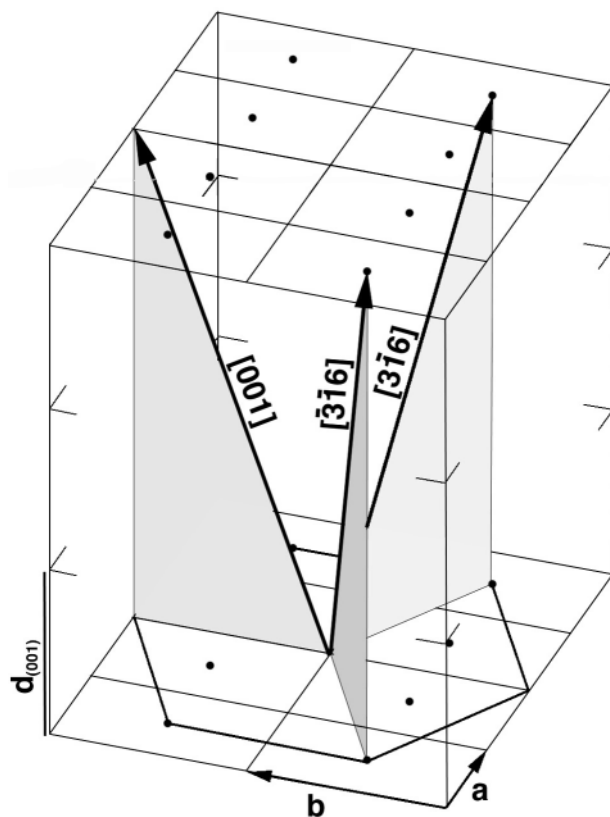
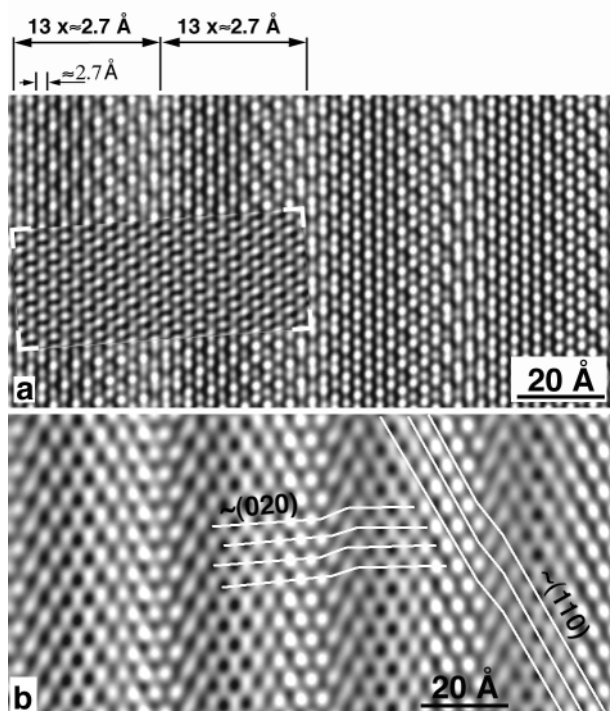


FIGURE 18. Sketch showing [001] and related directions  $[3\bar{1}6]$  and  $[\bar{3}16]$  relative to the subcell of antigorite. The large box has dimensions of  $4 \times 3 \times 2$  subcells, shown by the thin lines.

lographic effects mentioned three paragraphs earlier and conclude that the data in Table 3 provide an accurate description of the model structure of antigorite-*T*.

HRTEM images of both antigorite-*M* and antigorite-*T* (with  $n = 14$ ) taken along the  $[6\bar{1}3\bar{7}8]$  or  $[\bar{6}1378]$  directions resemble those along [001]. The main difference is that the number of (200) subcell planes ( $d_{hkl} = 2.7$  Å) equals  $m$  in a modulation period in [001] images and  $n$  in the other projections. As in the case of the antigorite-*T* with  $n = 14$  in Figure 20a, the  $[6\bar{1}3\bar{7}8]$  HRTEM image shows 13 fringes with spacings of  $\sim 2.7$  Å in a period perpendicular to the modulation. A calculated image is inserted in Figure 20a to allow comparison with the experimental one.

In spite of the seeming similarities between the [001] and  $[6\bar{1}3\bar{7}8]$  HRTEM images, the planes having  $d_{hkl}$  values near to  $d_{020}$  ( $\sim 4.6$  Å) of the subcell do not represent the T sheets of antigorite-*T*. Although Figures 7b and 20b of [001] and  $[6\bar{1}3\bar{7}8]$  projections of a sample of antigorite-*T* look alike, inflections instead of offsets occur in the  $[6\bar{1}3\bar{7}8]$  projection. These inflections resemble the {110} offsets in the Kunze model (Fig.



**FIGURE 20.** (a)  $[\bar{6}\bar{1}3\ 78]$  HRTEM image of an antigorite-*T* ( $n = 14$ ) at resolution of 2.2 Å (Deligh quarry) with an inserted calculated HRTEM image (sample thickness = 154 Å; radius of objective aperture = 0.45 Å<sup>-1</sup>;  $\Delta f = 200$  Å). There are 13 fringes with spacings of  $\sim 2.7$  Å in a period perpendicular to the modulation. (b) Reduced-resolution image (3 Å) of (a). The white lines indicate the inflections in the (020) and (110) subcell fringes.

6), but inflections occur in the (020) and (110) fringes, referred to the subcell in  $[\bar{6}\bar{1}3\ 78]$  antigorite-*T*.

We found that the image calculations for antigorite-*T* with  $n = 14$  also provide good matches to corresponding experimental images for antigorite-*T* with  $n > 14$ . However, analogous structures also occur in crystals with  $n > 14$ , and their  $[\bar{3}\bar{1}6]$  and  $[\bar{3}\bar{1}6]$  projections, referred to the subcell, are basically similar to those of the antigorite-*T* images discussed above. Figure 21 is an HRTEM image of antigorite-*T* with  $n = 20$  viewed down  $[\bar{3}\bar{1}6]$  of the subcell. For this and similar cases we use the calculated  $n = 14$  images for a part of the full modulation of the larger cells (Fig. 21).

There are some unavoidable limitations in antigorite image simulations. Stacking disorder provides a complication in both antigorite-*M* and antigorite-*T*. Problems also arise in the multislice calculations because of the large antigorite periodicities. For example, the repeat distance along  $[\bar{3}\bar{1}6]$  of the subcell equals 616 Å for antigorite-*T* with  $n = 14$ . However, a sample thickness of  $\sim 100$  Å is convenient for HRTEM but represents only a part of a repeat distance. As a result the calculated images, which are of necessity for integral numbers of repeat distances, can only provide an approximation of the experimental images.

Differences between the calculated and experimental images provide information about the locations where the structural model needs further adjustment. Minor differences

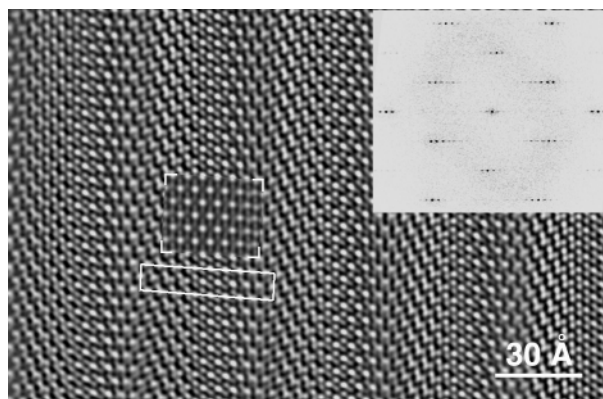


**FIGURE 21.**  $[\bar{6}\bar{1}3\ 78]$  HRTEM image of an antigorite-*T* ( $n = 20$ ; Felsőcsatár). The calculated diffraction pattern is in the upper-right corner. The inserted calculated image for  $n = 14$  matches the central part of the larger cell (marked by a white box) in the experimental image.

between experimental images and those calculated from our model can be seen along the arrowed positions of Figures 17 and 19. These differences occur in the areas of the O-sheet offsets, as can also be seen by reference to Figure 13c. We believe that the differences arise from different cation-cation separations (indicated by the bolded Mg atoms in Tables 2 and 3) relative to those away from the O-sheet offsets.

The fluctuating changes in contrast of the half-waves are prominent features of all the experimental images. These fluctuations, which are more subdued in the calculated images, can be seen in Figures 17 and 19 as alternating vertical bands of dark and light contrast. Kunze (1961) discussed possible and probable half-wave profiles that deviate from a cylinder profile; such deviations may result in the observed contrast fluctuations in our HRTEM images. We believe this contrast difference between experimental and calculated images arises from the implicit assumption in the calculations that cation sites lie along a curve that can be represented as a cylindrical section. However, the actual sites may lie along a surface that is better approximated by a slightly flattened cylinder. Moreover, the half-wave may be positioned so that it is only roughly symmetrical about either the semi-major or semi-minor axis of the flattened cylinder.

Both the *M* and *T* varieties appear identical in HRTEM images when viewed down  $[010]$ . The  $b/3$  displacements of adjacent layers in antigorite-*T* is the most important structural difference from antigorite-*M* with the same number of T positions. As the displacement is parallel to the viewing direction, no difference can be expected to be visible in the  $[010]$  antigorite images. Figure 22 shows such an HRTEM image; the inserted calculated image matches the experimental one, which is from the same crystal whose SAED pattern is shown in Figure 9. The streaking parallel to  $c^*$  in  $[010]$  SAED patterns arises from stacking effects, which will be considered in a separate paper.

Consideration of Figures 17 and 19 to 22 shows that there are acceptable matches, within experimental error, between the respective experimental images and the inserted ones that were

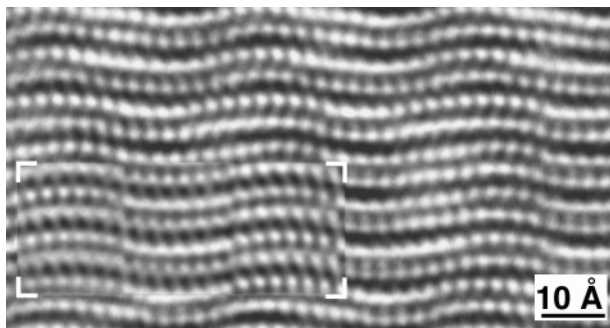


FIGURE 22. [010] HRTEM image of antigorite ( $n = 14$ ; Deligh quarry). The inserted calculated image matches the experimental one. (Sample thickness = 43.6 Å; radius of objective aperture = 0.45 Å<sup>-1</sup>;  $\Delta f = 275$  Å).

calculated using our new models. We take these matches as confirmations of the new features in our proposed structural models: (1) depending on the modulation wavelengths and the occurrence of  $b/3$  stackings of adjacent layers, either monoclinic or triclinic crystals can occur; (2) the four- and eight-membered silicate rings of all previous models do not, in fact, exist; and (3) only half of the number of octahedral offsets occur relative to those of previous models. In addition, by using high-resolution images, we were able to image the number of T and O sites and thereby directly estimate the compositions of specific, individual antigorite crystals.

#### ACKNOWLEDGMENTS

Electron microscopy was completed at the Center for High Resolution Electron Microscopy at Arizona State University. Major financial support came through a grant from the Earth Sciences Division of the National Science Foundation. The preliminary work in Hungary was supported by Ministry of Education grant no. FKFP 0202/1997. We thank J. Li for her kind assistance with the analytical electron microscopy. The manuscript benefited from constructive reviews by M. Mellini and an anonymous reviewer.

#### REFERENCES CITED

- Anselmi, B., Mellini, M., and Viti, C. (2000) Chlorine in the Elba, Monti Livornesi and Murlo serpentines: evidence for sea-water interaction. *European Journal of Mineralogy*, 12, 137–146.
- Bonatti, E. (1976) Serpentine protrusions in the oceanic crust. *Earth and Planetary Science Letters*, 32, 107–113.
- Brearley, A.J., Hanowski, N.P., and Whalen, J.F. (1999) Fine-grained rims in CM carbonaceous chondrites: A comparison of rims in Murchison and ALH 81002. *Lunar and Planetary Science Conference XXX*, Abstract no. 1460 (CD-ROM).
- Bunch, T.E. and Chang, S. (1980) Carbonaceous chondrites II: Carbonaceous chondrite phyllosilicates and light element geochemistry as indicators of parent body processes and surface conditions. *Geochimica et Cosmochimica Acta*, 44, 1543–1578.
- Buseck, P.R. and Hua, X. (1993) Matrices of carbonaceous chondrite meteorites. *Annual Reviews of Earth and Planetary Sciences*, 21, 255–305.
- Chapman, J.A. and Zussman, J. (1959) Further electron optical observations on crystals of antigorite. *Acta Crystallographica*, 12, 550–552.
- Christensen, N.I. (1972) The abundance of serpentinites in the oceanic crust. *Journal of Geology*, 80, 709–719.
- Dódony, I., Pósfai, M., and Buseck, P.R. (1998) Structural study of antigorite based on HRTEM image processing. 17th Meeting of the International Mineralogical Association, Toronto, IMA Abstracts.
- Francis, T.J.G. (1981) Serpentinization faults and their role in the tectonics of slow spreading ridges. *Journal of Geophysical Research*, 86, 11,616–11,622.
- Hyndman, R.D., Yamano, M., and Oleskevich, D.A. (1997) The seismogenic zone of subduction thrust faults. *The Island Arc*, 6, 244–260.
- Krstanovic, I. and Karanovic, L. (1995) Crystal structures of two lizardites, Mg<sub>3</sub>(Si<sub>2</sub>O<sub>7</sub>(OH)<sub>4</sub>). *Neues Jahrbuch für Mineralogie Monatshefte*, H50, 193–201.
- Kunze, W.G. (1956) Die Gewellte Struktur der Antigorits. I. *Zeitschrift für Kristallographie*, 108, 82–107.
- (1958) Die Gewellte Struktur der Antigorits. II. *Zeitschrift für Kristallographie*, 110, 282–320.
- (1961) Antigorit. *Fortschritte der Mineralogie*, 39, 206–324.
- Mellini, M. (1982) The crystal structure of lizardite-1T: Hydrogen bonds and polytypism. *American Mineralogist*, 67, 587–598.
- Mellini, M. and Viti, C. (1994) Crystal structure of lizardite-1T from Elba, Italy. *American Mineralogist*, 79, 1194–1198.
- Mellini, M. and Zanazzi, P.F. (1987) Crystal structure of lizardite-1T and lizardite-2H1 from Coli, Italy. *American Mineralogist*, 72, 943–948.
- Mellini, M. and Zussman, J. (1986) Carlosturanite (not ‘picrolite’) from Taberg, Sweden. *Mineralogical Magazine*, 50, 675–679.
- Mellini, M., Trommsdorf, V., and Compagnoni, R. (1987) Antigorite polysomatism: behaviour during progressive metamorphism. *Contributions to Mineralogy and Petrology*, 97, 147–155.
- Meyer, C., Leber, M., and Krivanek, O. (1996) Digital Micrograph 2.5.7, GATAN Inc.
- Moore, D.E., Lockner, D.A., Summers, R., Ma, S., and Byerlee, J.D. (1996) Strength of chrysotile-serpentine gouge under hydrothermal conditions: Can it explain a weak San Andreas fault? *Geology*, 24, 1041–1044.
- Moore, D.E., Lockner, D.A., Ma, S., Summers, R., and Byerlee, J.D. (1997) Strengths of serpentine gouges at elevated temperatures. *Journal of Geophysical Research*, 102, 14,787–14,801.
- O’Hanley, D.S. (1996) Serpentinites, records of tectonic and petrological history, 277 p. Oxford University Press, New York.
- Otten, M.T. (1993) High resolution transmission electron microscopy of polysomatism and stacking defects in antigorite. *American Mineralogist*, 78, 75–84.
- Peacock, S.M. (1987) Serpentinization and infiltration metasomatism in the Trinity peridotite, Klamath province, northern California: implications for subduction zones. *Contributions to Mineralogy and Petrology*, 95, 55–70.
- Peacock, S.M. and Hyndman, R.D. (1999) Hydrous minerals in the mantle wedge and the maximum depth of subduction thrust earthquakes. *Geophysical Research Letters*, 26, 2517–2520.
- Reinen, L.A., Weeks, J.D., and Tullis, T.E. (1991) The frictional behaviour of serpentinite: Implications for aseismic creep on shallow crustal faults. *Geophysical Research Letters*, 18, 1921–1924.
- (1994) The frictional behaviour of lizardite and antigorite serpentinites: Experiments, constitutive models, and implications for natural faults. *Pure and Applied Geophysics*, 143, 317–358.
- Spinnler, G.E. (1985) HRTEM study of antigorite, pyroxene-serpentine reactions, and chlorite, 248 p. Ph.D. dissertation, Arizona State University, Tempe.
- Thomas, J.M., Jefferson, D.A., Mallinson, L.G., Smith, D.J., and Crawford S.E. (1979) The elucidation of the ultrastructure of silicate minerals by high resolution electron microscopy and X-ray emission microanalysis. *Chemica Scripta*, 14, 167–179.
- Tomeoka, K. and Buseck, P.R. (1985) Indicators of aqueous alteration in CM carbonaceous chondrites: Microtextures of a layered mineral containing Fe, S, O and Ni. *Geochimica et Cosmochimica Acta*, 49, 2149–2163.
- (1990) Phyllosilicates in the Mokoia CV carbonaceous chondrite: Evidence for aqueous alteration in an oxidizing environment. *Geochimica et Cosmochimica Acta*, 54, 1745–1754.
- Thompson, J.B. (1978) Biopyriboles and polysomatic series. *American Mineralogist*, 63, 239–249.
- Uehara, S. (1998) TEM and XRD study of antigorite superstructures. *Canadian Mineralogist*, 36, 1595–1605.
- Uehara, S. and Shirozu, H. (1985) Variations in chemical compositions and structural properties of antigorites. *Mineralogical Journal (Japan)*, 12, 299–318.
- Viti, C. and Mellini, M. (1998) Mesh textures and bastites in the Elba retrograde serpentinites. *European Journal of Mineralogy*, 10, 1341–1359.
- (1996) Vein antigorites from Elba Island, Italy. *European Journal of Mineralogy*, 8, 423–434.
- Wicks, F.J. and Whittaker, E.J.W. (1975) A reappraisal of the structures of the serpentine minerals. *Canadian Mineralogist*, 13, 227–243.
- Wicks, F.J. and O’Hanley, D.S. (1988) Serpentine minerals: Structures and petrology. In S.W. Bailey, Ed., *Hydrous Phyllosilicates (Exclusive of Micas)*, vol. 19, p. 91–159. Reviews in Mineralogy, Mineralogical Society of America, Washington, D.C.
- Wunder, B., Baronnat, A., and Schreyer, W. (1997) Ab-initio synthesis and TEM confirmation of antigorite in the system MgO-SiO<sub>2</sub>-H<sub>2</sub>O. *American Mineralogist*, 82, 760–764.
- Yada, K. (1979) Microstructures of chrysotile and antigorite by high-resolution electron microscopy. *Canadian Mineralogist*, 17, 679–691.
- Zolensky, M., Barrett, R., and Browning, L. (1993) Mineralogy and composition of matrix and chondrule rims in carbonaceous chondrites. *Geochimica et Cosmochimica Acta*, 57, 3123–3148.

MANUSCRIPT RECEIVED FEBRUARY 6, 2001

MANUSCRIPT ACCEPTED JUNE 26, 2002

MANUSCRIPT HANDLED BY ADRIAN J. BREARLEY